The Astrophysical Journal, 725:1405–1420, 2010 December 20 doi:10.1088/0004-637X/725/2/1405

CLOUDS IN THE COLDEST BROWN DWARFS: FIRE SPECTROSCOPY OF ROSS 458C*

Adam J. Burgasser[1,2,7], Robert A. Simcoe[2,8], John J. Bochanski[2], Didier Saumon[3], Eric E. Mamajek[4], Michael C. Cushing[5], Mark S. Marley[6], Craig McMurtry[4], Judith L. Pipher[4], and William J. Forrest[4]
[1] Center for Astrophysics and Space Science, University of California San Diego, La Jolla, CA 92093, USA; aburgasser@ucsd.edu
[2] Massachusetts Institute of Technology, Kavli Institute for Astrophysics and Space Research, Building 37, Room 664B, 77 Massachusetts Avenue, Cambridge, MA 02139, USA
[3] Los Alamos National Laboratory, P.O. Box 1663, MS F663, Los Alamos, NM 87545, USA
[4] Department of Physics and Astronomy, University of Rochester, Rochester, NY 14627, USA
[5] Jet Propulsion Laboratory, California Institute of Technology, Pasadena, CA, USA
[6] NASA Ames Research Center, Mail Stop 245-3, Moffett Field, CA 94035, USA
Received 2010 August 16; accepted 2010 September 28; published 2010 November 29

ABSTRACT

Condensate clouds are a salient feature of L dwarf atmospheres, but have been assumed to play little role in shaping the spectra of the coldest T-type brown dwarfs. Here we report evidence of condensate opacity in the near-infrared spectrum of the brown dwarf candidate Ross 458C, obtained with the Folded-Port Infrared Echellette (FIRE) spectrograph at the Magellan Telescopes. These data verify the low-temperature nature of this source, indicating a T8 spectral classification, $\log_{10} L_{\rm bol}/L_\odot = -5.62 \pm 0.03$, $T_{\rm eff} = 650 \pm 25$ K, and a mass at or below the deuterium burning limit. The data also reveal enhanced emission at the *K* band associated with youth (low surface gravity) and supersolar metallicity, reflecting the properties of the Ross 458 system (age = 150–800 Myr, [Fe/H] = +0.2 to +0.3). We present fits of FIRE data for Ross 458C, the T9 dwarf ULAS J133553.45+113005.2, and the blue T7.5 dwarf SDSS J141624.08+134826.7B, to cloudless and cloudy spectral models from Saumon & Marley. For Ross 458C, we confirm a low surface gravity and supersolar metallicity, while the temperature differs depending on the presence (635^{+25}_{-35} K) or absence (760^{+70}_{-45} K) of cloud extinction. ULAS J1335+1130 and SDSS J1416+1348B have similar temperatures (595^{+25}_{-45} K), but distinct surface gravities ($\log g$ = 4.0–4.5 cgs versus 5.0–5.5 cgs) and metallicities ([M/H] $\approx$ +0.2 versus −0.2). In all three cases, cloudy models provide better fits to the spectral data, significantly so for Ross 458C. These results indicate that clouds are an important opacity source in the spectra of young cold T dwarfs and should be considered when characterizing planetary-mass objects in young clusters and directly imaged exoplanets. The characteristics of Ross 458C suggest that it could itself be regarded as a planet, albeit one whose cosmogony does not conform with current planet formation theories.

Key words: brown dwarfs – planetary systems – stars: fundamental parameters – stars: individual (Ross 458C, ULAS J130041.72+122114.7, ULAS J133553.45+113005.2, SDSS J141624.08+134826.7B, ULAS J141623.94+134836.3) – stars: low-mass

Online-only material: color figures

1. INTRODUCTION

Mineral condensate clouds are a unique and prominent constituent of the atmospheres of the coldest brown dwarfs, the L dwarfs, and T dwarfs (Kirkpatrick 2005, and references therein). For the L dwarfs, condensates are a primary contributor to shaping spectral energy distributions (SEDs). Their formation depletes the atmosphere of TiO and VO gases, transforming optical SEDs and defining the L dwarf spectral sequence (Jones & Tsuji 1997; Kirkpatrick et al. 1999; Lodders 2002). Condensate opacity contributes to muted infrared H_2O bands and the characteristic red near-infrared colors of L dwarfs ($J - K$ = 1.5–2.5; Chabrier et al. 2000; Knapp et al. 2004). Evidence of silicate grain absorption has also been found in the mid-infrared spectra of L dwarfs (Cushing et al. 2006; Helling et al. 2006; Looper et al. 2008). For the T dwarfs, condensates appear to play a minor role, as evidenced by strong molecular gas absorption features and typically blue near-infrared colors ($J - K = -0.5$–0.5; Burgasser et al. 2002b, 2006b; Geballe et al. 2002; Cushing et al. 2005). This shift is believed to be the result of clouds sinking below the visible photosphere (Ackerman & Marley 2001; Cooper et al. 2003; Tsuji 2005) or breaking apart (Burgasser et al. 2002a; Marley et al. submitted), although the details of this transition remain poorly understood (Burrows et al. 2006; Burgasser 2007; Saumon & Marley 2008).

Even without considering condensates, modeling the highly structured SEDs of T dwarfs remains a challenge. The abundances and opacities of prominent gas species—H_2 (collision-induced absorption; Linsky 1969), H_2O, CH_4, NH_3, and neutral alkalis (pressure-broadened wings; Burrows & Volobuyev 2003)—are highly sensitive to photospheric gas conditions. Temperature and pressure variations, elemental abundances, and vertical mixing all have observable effects on T dwarf spectra (e.g., Knapp et al. 2004; Burgasser et al. 2006a; Saumon et al. 2007; Stephens et al. 2009). In principle, one could disentangle the contributions of these atmospheric properties on observed spectra and derive bulk characteristics—mass, age, and metallicity—for individual sources (e.g., Burgasser et al. 2006a; Leggett et al. 2009). However, a variety of effects drive systematic deviations between model and observed spectra. These include incomplete opacities for key absorbers such as CH_4, NH_3, and K I (e.g., Allard et al. 2003; Cushing et al. 2008; Freedman

* This paper includes data gathered with the 6.5 m Magellan Telescopes located at Las Campanas Observatory, Chile.
[7] Hellman Fellow.
[8] Alfred P. Sloan Foundation Research Fellow.

et al. 2008); non-equilibrium chemistry arising from vertical mixing (e.g., Saumon et al. 2006, 2007); metallicity effects on chemical pathways (e.g., Lodders & Fegley 2002; Burgasser et al. 2003; Visscher et al. 2010); and the influence of condensate clouds in regions of minimum gas opacity (e.g., Tsuji et al. 1999; Ackerman & Marley 2001; Burrows et al. 2002). These processes lead to persistent uncertainties in inferred atmospheric and physical parameters for individual sources (cf. Burningham et al. 2010; Burgasser et al. 2010b).

Benchmark T dwarfs, with independent determinations of age, mass, and metallicity, are important calibrators for brown dwarf atmospheric studies (Pinfield et al. 2006). Such benchmarks include widely separated T dwarf companions to nearby stars, several examples of which have been identified over the past 15 years (e.g., Nakajima et al. 1995; Burgasser et al. 2000; Luhman et al. 2007; Burningham et al. 2009). Most recently, Goldman et al. (2010) and Scholz (2010a) reported the discovery of a faint ($J = 16.67 \pm 0.01$), comoving candidate T dwarf companion to the Ross 458 system in the UKIRT Infrared Deep Sky Survey (UKIDSS; Lawrence et al. 2007). The source, ULAS J130041.72+122114.7 (hereafter Ross 458C), is separated by 102″ from the M0.5 Ve + M7 Ve Ross 458AB pair, implying a projected separation of over 1100 AU at a distance of 11.7 ± 0.2 pc (van Leeuwen 2007). The late-type nature of Ross 458C was inferred from its optical and near-infrared colors ($z-J = 3.55 \pm 0.19$; $J - K = -0.21 \pm 0.06$), faint absolute magnitude ($M_J = 16.40 \pm 0.04$) and large flux contrast in filters sampling the 1.6 μm CH_4 band (cf. Tinney et al. 2005). From these photometric measurements, Scholz (2010a) and Goldman et al. (2010) estimated spectral types of T7 ± 1 and T8−9 for Ross 458C, respectively. However, no spectrum was reported in either study.

If Ross 458C is a brown dwarf, it is a potentially interesting benchmark for several reasons. Kinematics of the Ross 458 system coincide with the Hyades supercluster (Eggen 1960; Montes et al. 2001), an extended population of relatively young and metal-rich stars that includes the 625 ± 50 Myr Hyades open cluster (Perryman et al. 1998). The primary exhibits conspicuous activity in Hα and Ca II lines (Browning et al. 2010) and is an X-ray source (Kiraga & Stepien 2007; López-Santiago et al. 2009). Ross 458C could therefore be a young and/or metal-rich brown dwarf benchmark, useful for constraining both evolutionary and atmospheric models (cf. Zapatero Osorio et al. 2004; Dupuy et al. 2009a).

In this paper, we present the first spectroscopic observations of Ross 458C, obtained in the near-infrared with the newly commissioned Folded-Port Infrared Echellette (FIRE; Simcoe et al. 2008). These data confirm the late-type T dwarf nature of the source and indicate a low surface gravity and supersolar metallicity consistent with characteristics of the primary. Furthermore, model fits indicate that cloud opacity plays a prominent role in shaping its near-infrared spectrum. In Section 2, we constrain the age and metallicity of the Ross 458 system based on the photometric, spectral, kinematic, and rotational properties of its M0.5 Ve primary. In Section 3, we describe our FIRE observations of Ross 458C and two other late-type T dwarfs, from which we derive spectral types and basic physical characteristics. In Section 4, we fit the spectral data for these three sources to cloudless and cloudy atmospheric models from Saumon & Marley (2008, hereafter SM08) and compare the inferred atmospheric and physical parameters to prior studies. In Section 5, we discuss the role of condensates in shaping the near-infrared SEDs of young, cold T dwarfs, and their influence on T dwarf temperature scales. In Section 6, we summarize our results.

2. CHARACTERIZING THE ROSS 458 SYSTEM

2.1. Examining Association with the Hyades Open Cluster

Under the assumption of coevality, some physical properties of Ross 458C can be inferred from its stellar companions, specifically age and metallicity. As such, it is necessary to examine the association of this system with the Hyades supercluster, a kinematic stream composed of several dozen nearby stars with similar space motions (Eggen 1960; Montes et al. 2001). While comoving associations typically have similar ages and compositions, the ages of the Hyades supercluster stars span the star formation history of the disk (0.4–2.0 Gyr; Famaey et al. 2005; Antoja et al. 2008), so stream membership is not a particularly useful age indicator. Within the stream is the eponymous Hyades open cluster, the nearest open cluster to the Sun, which constitutes a coeval group with an age of 625 ± 50 Myr (Perryman et al. 1998). Because of its proximity, the members of the Hyades cluster halo are distributed broadly across the sky. It is therefore not unreasonable for Ross 458 to be associated with this structure.

To examine this possibility, we calculated the systemic space velocity[9] of the Ross 458 system. We used the long-baseline proper motion from *Tycho-2* ($\mu_\alpha = -640.1 \pm 1.5$ mas yr^{-1}; $\mu_\delta = -25.1 \pm 1.4$ mas yr^{-1}; Høg et al. 2000), the radial velocity from Nidever et al. (2002, $V_r = -11.2 \pm 0.1$ km s^{-1}), and the revised *Hipparcos* parallax ($\pi = 85.5 \pm 1.5$ mas; van Leeuwen 2007). From these we find heliocentric $(U, V, W) = (30.6, -18.8, -9.9) \pm (0.5, 0.3, 0.2)$ km s^{-1}. The velocity of the Hyades cluster in the same coordinate system (de Bruijne et al. 2001) is $(U, V, W) = (42.25, -19.06, -1.45) \pm (0.14, 0.13, 0.21)$ km s^{-1}, a difference of $(11.7, -0.3, 8.5) \pm (0.5, 0.3, 0.3)$ km s^{-1} (see also Perryman et al. 1998). This is much larger than the one-dimensional velocity dispersion of Hyades cluster members, ∼0.35 km s^{-1} (Madsen 2003), amounting to a $\sim 20\sigma$ discrepancy. Hence, Ross 458 is not currently kinematically associated with the Hyades open cluster.

Has Ross 458 ever been associated with the Hyades cluster? Its current separation from the cluster center is 53 pc. Using the epicyclic orbit approximation to model the past orbits of Ross 458 and the Hyades (adopting the Oort parameters of Feast & Whitelock 1997 and local standard of rest from Dehnen & Binney 1998), we find that Ross 458 was never closer to the Hyades than ∼50 pc during the past 100 Myr, or about 5 tidal radii. Hence, there is no evidence of past or present physical association between Ross 458 and the Hyades open cluster, and association with the Hyades supercluster provides no meaningful constraint on the age of this system.

2.2. The Age of the Ross 458 System

Despite the wide range of ages associated with the Hyades kinematic stream, there is considerable evidence that the Ross 458 system itself is quite young. The M0.5 Ve primary[10] (Reid et al. 1995) is an "ultra-fast rotator" with a period between 1.54 and 2.89 days (Pizzolato et al. 2003; Kiraga & Stepien

[9] We adopted a heliocentric, right-handed rectangular coordinate system with U velocity locally pointing toward the Galactic center, V velocity pointing in the direction of Galactic rotation ($\ell, b = 90°, 0°$), and W velocity pointing toward the north Galactic pole ($b = +90°$).

[10] The M dwarf components of Ross 458 are separated by 0.″5 (Beuzit et al. 2004), implying that reported optical spectroscopy of this system probably includes both components. However, Ross 458B is ≈8 mag fainter at V (Section 2.3), implying that its contribution to combined light optical spectra is negligible.

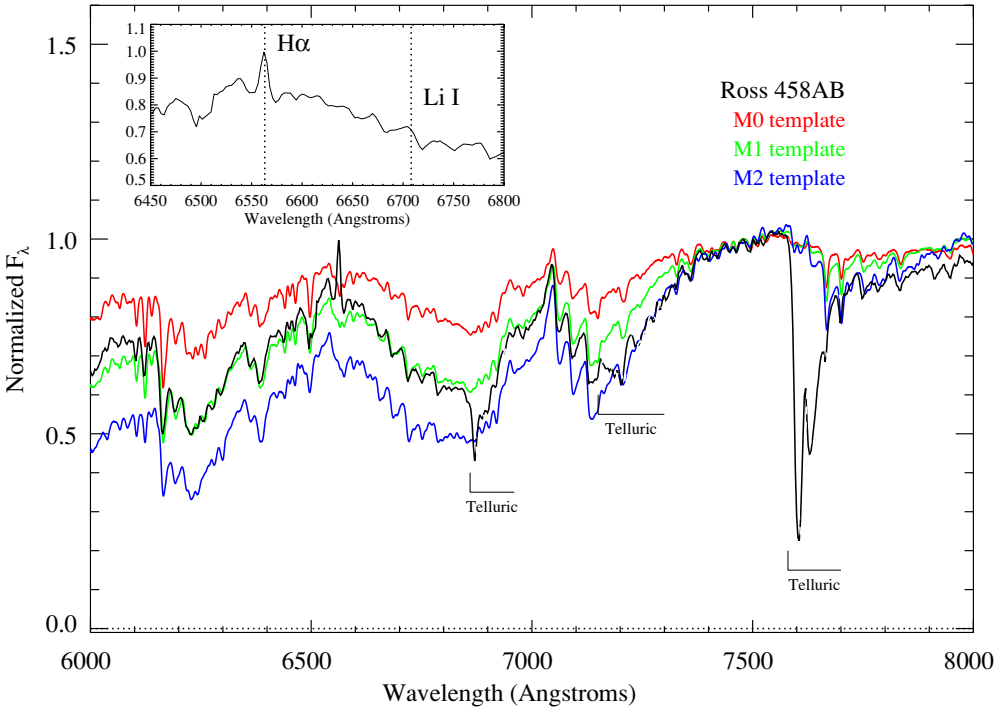

Figure 1. Red optical spectrum of Ross 458AB (black line) compared to M0 (red line), M1 (green line), and M2 (blue line) spectral templates from Bochanski et al. (2007). All spectra are normalized at 7500 Å, and templates are smoothed to the resolution of the observational data ($\lambda/\Delta\lambda \approx 800$) using a Gaussian kernel. Regions of strong telluric absorption in the observational data are indicated. The inset box details the 6450–6800 Å region highlighting the prominent Hα emission and the absence of Li I absorption.

(A color version of this figure is available in the online journal.)

2007). Ross 458A had the highest measured projected rotational velocity ($v \sin i = 9.7 \pm 0.5$ km s^{-1}) among 69 nearby M0–M3 dwarfs in the California Planet Search program, in which only ~3% of early-M dwarfs had any detectable rotation ($v \sin i \gtrsim 3$ km s^{-1}; Browning et al. 2010). Beuzit et al. (2004) have argued for an age less than 1 Gyr on the basis of this rotation.

In addition, Ross 458A exhibits strong magnetic activity. The presence of Hα emission indicates an upper activity age limit of 400–800 Myr (West et al. 2008). This limit is roughly consistent with the analysis of Takeda et al. (2007), who deduce a 68% upper limit of 440 Myr based on theoretical modeling of the primary's high-resolution spectrum (however, this does not appear to be a "well-defined" age according to that study). Ross 458 is also an X-ray source, detected in three Röntgen Satellite (*ROSAT*) Position Sensitive Proportional Counter (PSPC) pointings and in the All-Sky Survey (Voges et al. 2000). Combining these four observations yields a mean *ROSAT* PSPC flux in the 0.1–2.4 keV band of 4.35 counts s^{-1}, and mean hardness ratios of HR1 = −0.13 and HR2 = −0.09. The mean X-ray flux, coupled with the energy conversion factors of Fleming et al. (1995) and the *Hipparcos* parallax, implies a soft X-ray luminosity of $L_X = 5 \times 10^{29}$ erg s^{-1} and an X-ray to bolometric luminosity ratio of $\log L_X/L_{\rm bol} = -2.7$. Such a high ratio defines Ross 458 as a "saturated" X-ray emitter, as expected for stars of similar color and rotation periods of $\lesssim$4 days (Pizzolato et al. 2003). The combination of color and rotation period for Ross 458A also classifies it as a C-sequence ("convective") rotator in the scheme of Barnes (2003). The characteristic spin-down timescale for such stars is ~300 Myr. From a cross comparison of age-dated cluster and field populations of low-mass, solar-type stars, Barnes (2003) concludes that the fraction of C-sequence ultra-fast rotators reduces to zero by age ~800 Myr. Hence, this age can be considered a robust upper limit for the Ross 458 system that is consistent with activity estimates.

A lower limit on the age of this system can be inferred from the optical spectrum of the primary. Figure 1 displays $\lambda/\Delta\lambda \approx 800$ optical spectroscopy for the combined AB components obtained by J. D. Kirkpatrick with the CTIO 1.5 m RC Spectrograph on 1996 May 22.[11] The spectrum is compared to M0, M1, and M2 spectral templates from Bochanski et al. (2007), the M1 showing the strongest agreement with the data. The prominent 6563 Å Hα line is clearly seen in these data, but there is no indication of Li I absorption at 6708 Å, implying an age older than 30–50 Myr (Magazzu et al. 1993; Chabrier et al. 1996; Bildsten et al. 1997). Furthermore, there is no indication low surface gravity features, such as the weakened 7700 Å K I doublet lines observed of cooler young M dwarfs up to the age of the Pleiades (e.g., Martin et al. 1996; Kirkpatrick et al. 2008). These spectroscopic constraints place a lower limit on the age of this system of ~150 Myr.

2.3. The Metallicity of the Ross 458 System

The metallicity of Ross 458A can be determined from its position on the $V - K/M_K$ color magnitude diagram (CMD), a combination that effectively segregates mass and metallicity variations in field M dwarfs (Bonfils et al. 2005; Johnson & Apps 2009; Schlaufman & Laughlin 2010). For better accuracy, we disentangled the flux of Ross 458A from its closely separated M7 companion. Using $\Delta K = 4.41$ from Beuzit et al. (2004, a 0.1 mag uncertainty is assumed), we determined $M_{K_A} = 5.26 \pm 0.04$ and $M_{K_B} = 9.67 \pm 0.11$. We then used unresolved *Hipparcos*/Two Micron All Sky Survey (2MASS) photometry ($V - K = 4.180 \pm 0.016$) and the mean $V - K/M_K$ relation

[11] These data are available at DwarfArchives, http://www.dwarfarchives.org.

Table 1
Magellan/FIRE Observing Log

Source	SpT	UKIDSS *J*	Date (UT)	Airmass	t_{int}[a]	A0 V Calibrator
Ross 458C	T8	16.69 ± 0.01	2010 Apr 3	1.34–1.36	642	HD 114381
ULAS J133553.45+113005.2	T9	17.90 ± 0.01	2010 Apr 7	1.38–1.42	642	HD 114381
ULAS J141623.94+134836.3[b]	T7.5p	17.35 ± 0.02	2010 Apr 6	1.40–1.44	642	HD 124773

Notes.
[a] Total integration time divided into four ABBA dithered pointings. Total integration includes 10.61 s frame readout.
[b] aka SDSS J141624.08+134826.7B.

of Schlaufman & Laughlin (2010) to estimate $\Delta V = 7.93 \pm 0.14$ and hence $(V - K)_A = 4.16 \pm 0.02$. The M_K/metallicity calibration of Johnson & Apps (2009) then yields [Fe/H] = +0.31 ± 0.05, while the $V - K$/metallicity calibration of Schlaufman & Laughlin (2010) yields [Fe/H] = +0.20 ± 0.05. Hence, both relations indicate a supersolar metallicity for the Ross 458 system. However, these quantitative estimates should be regarded with care given the young age of the system. The primary may be systematically brighter/redder than the control samples used by Johnson & Apps (2009) and Schlaufman & Laughlin (2010), resulting in a systematically higher metallicity.

In summary, the Ross 458 system has a probable age of 150–800 Myr based on its rotation, strong activity indicators, and spectroscopic features. It also appears to be metal-rich, with [Fe/H] = +0.2 to +0.3, albeit with possible age biases. We will compare these values to results from spectral modeling of the T dwarf companion in Section 4.

3. NEAR-INFRARED SPECTROSCOPY

3.1. The FIRE Spectrograph

FIRE is a cross-dispersed, near-infrared spectrometer recently installed at the auxiliary Nasmyth focus of the Magellan 6.5 m Baade Telescope. It is a single-object spectrograph, designed primarily to deliver moderate-resolution ($\lambda/\Delta\lambda \approx 6000$ for a 0.″6 wide slit) spectra over the 0.85–2.5 μm range in a single exposure. The 21 orders dispersed by a combination of prisms and reflection grating are imaged onto a 2048 × 2048, HAWAII-2RG (H2RG) focal plane array. A mirror can also be rotated in place of the reflection grating to obtain a single-order, high-throughput spectrum at lower resolution ($\lambda/\Delta\lambda$ = 250–350; see below). A second H2RG camera images the entrance slit through an MKO[12] *J*-band filter for source acquisition and manual guiding. Further details on this instrument can be found in Simcoe et al. (2008, 2010) and on the instrument Web page.[13]

3.2. Observations and Data Reduction

Data presented here were obtained during FIRE's commissioning run during March 31 through 2010 April 7 (UT). Observations were obtained for three T dwarfs: Ross 458C, the T7.5 ULAS J141623.94+134836.3 (aka SDSS J141624.08+134826.7B and hereafter SDSS J1416+1348B; Burningham et al. 2010; Scholz 2010b; Burgasser et al. 2010b), and the T9 ULAS J133553.45+113005.2 (hereafter ULAS J1335+1130; Burningham et al. 2008). A summary of the observations is given in Table 1. Conditions ranged from clear (April 3 and 7) to patchy cirrus (April 6), with seeing of 0.″6–0.″8 at the *J* band. For all sources, we employed FIRE's prism-dispersed mode with the 0.″6 wide slit aligned to the parallactic angle (rotator angle 89.°5). The resolution for this setting ranges from $\lambda/\Delta\lambda \approx 350$ in the 1.0–1.4 μm *Y*- and *J*-band region to $\lambda/\Delta\lambda \approx 250$ in the 1.4–2.5 μm *H*- and *K*-band region, as determined from Gaussian fits to emission lines in the arc lamp spectra and telluric emission lines in the science images. The spectrograph detector was read out using the four-amplifier mode at "high gain" (1.2 counts/e^-). Each source was observed in four 150 s exposures using an ABBA dither pattern, nodding 9″ along the 30″ slit, followed by the observation of a nearby A0 V star at similar airmass for telluric correction and flux calibration. Exposures of arc lamps (HeNeAr on April 3; NeAr on April 6 and 7) and quartz lamps, reflected off of the Baade secondary screen, were obtained with the target and A0 V stellar observations for wavelength and pixel response calibration.

Data were reduced using a combination of standard IRAF[14] and custom IDL[15] routines. A pixel response frame was first constructed by combining two quartz lamp images taken with the lamp at high (2.5 V) and low (1.5 V) voltage settings. This was necessary to compensate for the substantial thermal emission from the lamp screen which tended to saturate the detector at the longest wavelengths. The two images were stitched together at column 1300 (roughly 1.4 μm), then normalized by a median combination of all columns along the dispersion region, which eliminated the intensity step function at the stitch and isolated pixel-to-pixel response variations. The science images were divided by this pixel response frame, and bad pixels interpolated by averaging over nearest neighbors. The images were then pairwise subtracted to remove sky background. Spectra were extracted using the IRAF *apall* task. Calibrator stars were extracted first, then used as traces for the T dwarf and arc lamp spectra. A wavelength solution was generated from a fifth-order spline fit to 60 lines in the arc lamp spectra using the IRAF task *identify*, producing a mean dispersion of 8.5 Å pixel^{-1} and scatter of 9 Å (≈1 pixel). Note that the actual dispersion varies considerably along the chip, from 4 Å pixel^{-1} at 1.0 μm to 20 Å pixel^{-1} at 2.4 μm. The individual spectra were combined using the *xcombspec* routine from SpeXtool (Cushing et al. 2004), using a robust weighted mean after normalizing in the 1.2–1.4 μm region. The SpeXtool task *xtellcor_general* was used to compute telluric correction and flux calibration from the A0 V star, following the prescription of Vacca et al. (2003) and assuming a line profile width of 18 Å.

To verify the flux calibration of our data, we computed MKO spectrophotometric colors from all three sources from the FIRE spectra following Cushing et al. (2005), computing

[12] Mauna Kea Observatory filter system; see Tokunaga et al. (2002) and Simons & Tokunaga (2002).
[13] http://www.firespectrograph.org

[14] Image Reduction and Analysis Facility (IRAF; Tody 1986) is distributed by the National Optical Astronomy Observatory, which is operated by the Association of Universities for Research in Astronomy, Inc., under cooperative agreement with the National Science Foundation.
[15] Interactive Data Language.

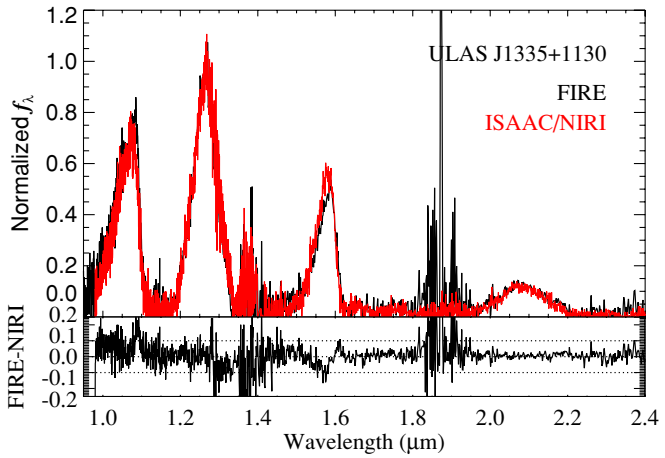

Figure 2. Spectral observations of ULAS J1335+1130 based on Magellan/FIRE (this study) and Gemini-North/NIRI plus VLT/ISAAC (Burningham et al. 2008, red line). Both spectra are normalized at the 1.27 μm flux peak. The difference between these spectra (bottom panel) is less than 10% over most of the near-infrared band.

(A color version of this figure is available in the online journal.)

100 iterations with each spectrum varied by its noise spectrum to determine uncertainties. For ULAS J1335+1130 and SDSS J1416+1348B, these colors match UKIDSS photometry to within the uncertainties, indicating robust relative flux calibration. For Ross 458C, the MKO colors are intermediate between the UKIDSS and ground-based GROND (Greiner et al. 2008) photometry reported in Goldman et al. (2010), which themselves differ significantly (UKIDSS $J - K = 0.51 \pm 0.06$; GROND $J - K = -0.21 \pm 0.06$). This discrepancy may be due to differences in the filter passbands between UKIDSS, MKO, and GROND filter passbands or may reflect intrinsic variability in the source. In Figure 2, we compare our reduced FIRE spectrum of ULAS J1335+1130 to that obtained by Burningham et al. (2008) using the Gemini-North Near-Infrared Imager and Spectrometer (NIRI; Hodapp et al. 2003) and Paranal Very Large Telescope Infrared Spectrometer and Array Camera (ISAAC; Moorwood et al. 1998). The Burningham et al. spectrum was stitched together from four orders individually flux calibrated using UKIDSS *YJHK* photometry. Our spectrum is in excellent agreement with the NIRI and ISAAC data, with deviations of less than 10% outside the telluric absorption regions. Importantly, the FIRE data reproduce the relative *YJHK* flux peaks, which are essential for spectral model fits (Section 4).

3.3. Results

Figure 3 displays the reduced spectrum of Ross 458C, scaled to its absolute flux (F_ν units at 10 pc) based on UKIDSS *J*-band photometry and the *Hipparcos* parallax of the Ross 458 system. Signal-to-noise ratio (S/N) in the spectrum ranges from 50 to 80 in each of the *YJHK* flux peaks. Ross 458C exhibits the classic spectral signatures of a T dwarf, with strong H_2O and CH_4 absorption bands at 1.15, 1.4, 1.6, 1.8, and 2.2 μm; a steep red optical slope shaped by the pressure-broadened 0.77 μm K I wings; and a relatively blue SED from 1.2 to 2.1 μm, due in part to collision-induced H_2 absorption (Linsky 1969; Saumon et al. 1994; Borysow 2002). As anticipated from its extreme CH_4-filter colors, the 1.6 μm CH_4 band of Ross 458C is quite deep, while the *J*- and *H*-band flux peaks are narrow, all indicative of a very late-type, low-temperature T dwarf. Indeed, as shown in Figure 4, these features in the spectrum of Ross 458C are intermediate between those of SDSS J1416+1348B and ULAS J1335+1130, indicating an intermediate spectral type.

Our spectrum of Ross 458C also reveals the presence of the 1.24/1.25 μm K I doublet, highlighted in the inset box of Figure 3. These lines are known to fade in the latest-type T dwarfs (Burgasser et al. 2002b; McLean et al. 2003), likely a consequence of KCl(g) formation at temperatures below 1000 K (Lodders 1999). We measured pseudoequivalent widths pEW = 2.7 ± 0.2 Å for each doublet line, comparable to measurements for other T7–T8 dwarfs (Burgasser et al. 2002b; McLean et al. 2003). We do not see these lines in our spectra of ULAS J1335+1130 or SDSS J1416+1348B to limits of 0.5 and 0.3 Å, respectively. For the latter source, this may be a consequence of its subsolar metallicity in analogy to the metal-poor T6 dwarf 2MASS J09373487+2931409 (Burgasser et al. 2002b; McLean et al. 2007; see Section 4.2).

Another feature of note in the spectrum of Ross 458C is its fairly pronounced 2.1 μm *K*-band peak. The relative brightness of this peak is greater than those of both ULAS J1335+1130 and SDSS J1416+1348B, in accord with its reddest $J - K$ color. The *K*-band peak is normally suppressed by H_2 absorption in late-type T dwarfs. This absorption is weakened in brown dwarfs with low surface gravities (i.e., young, low mass) and/or higher metallicities, as both effects result in a lower photospheric pressure and weaker collision-induced absorption. For Ross 458C, both of these properties likely contribute based on the characteristics of the system (Section 2).

3.4. Spectral Classification

To classify the T dwarfs, we used the near-infrared spectral indices and index-spectral-type relations defined in Burgasser et al. (2006b), Warren et al. (2007), and Burningham et al. (2008); these are listed in Table 2. Our index measurements for ULAS J1335+1130 and SDSS J1416+1348B are in rough agreement with previous results (Burningham et al. 2008, 2010; Burgasser et al. 2010b), with minor variances attributable to differences in spectral resolution and S/N between data sets. We derive mean classifications of T8, T8.5, and T7.5p for Ross 458C, ULAS J1335+1130, and SDSS J1416+1348B, respectively. Uncertainties of 0.5 subtypes are assumed for the first two sources, while the last classification is deemed "peculiar" due to the larger scatter in indices (±1.2 subtypes). The last two classifications formally agree with previously published results (Burningham et al. 2008, 2010; Burgasser et al. 2010b). Our classification of Ross 458C splits the difference between the photometric estimates of Scholz (2010a) and Goldman et al. (2010) and is consistent with the relative ordering of the spectra in Figure 4. The absolute *J* magnitude of Ross 458C is also comparable to other T8 dwarfs (Vrba et al. 2004).

3.5. Physical Properties of Ross 458C

With a spectral type and known distance, it is possible to assess some of the basic physical properties of Ross 458C. A bolometric luminosity was determined using the absolute UKIDSS *JHK*-band magnitudes and bolometric corrections (BC) from Liu et al. (2010). Adopting[16] $BC_J = 2.62 \pm 0.14$, $BC_H = 2.19 \pm 0.07$, and $BC_K = 2.05 \pm 0.09$ for a T8

[16] Error estimates quoted here take into account uncertainties in the spectral classification (±0.5 subtype), photometry, parallax of Ross 458, and the spectral-type/BC relations (0.14, 0.07, and 0.08 mag for *J*, *H*, and *K*, respectively). Systematic errors—e.g., from gravity or metallicity effects—are not accounted for.

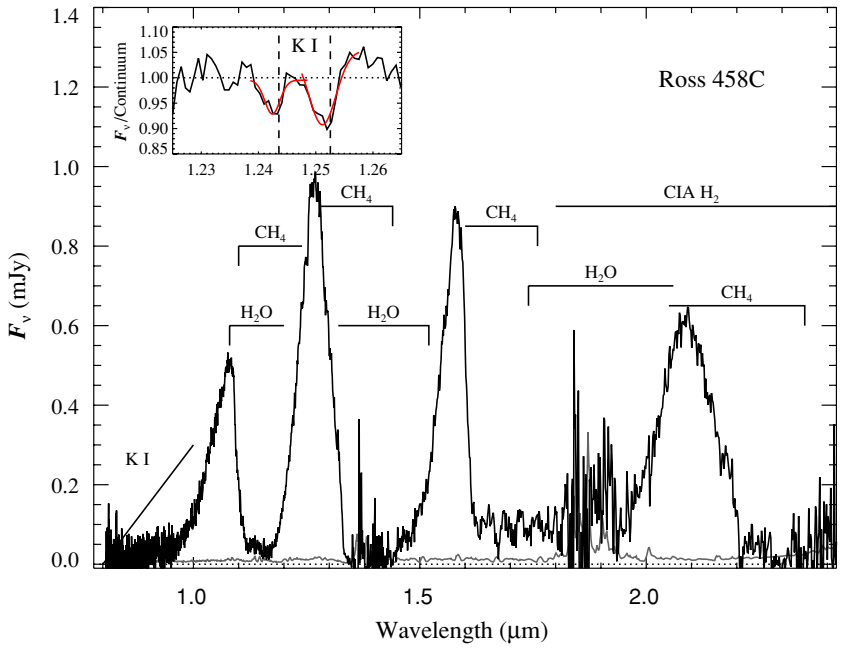

Figure 3. FIRE prism spectrum of Ross 458C in absolute flux units (F_ν). The uncertainty spectrum is indicated by the gray line. Prominent H_2O and CH_4 absorption features are labeled, as well as regions influenced by the pressure-broadened K I doublet wing ($\lambda \lesssim 1$ μm) and collision-induced H_2 opacity ($\lambda \gtrsim 1.75$ μm). The inset box shows continuum-normalized flux between 1.23 and 1.26 μm, highlighting the weak 1.24/1.25 μm K I doublet present in the spectrum of this source (red lines show Gaussian fits).

(A color version of this figure is available in the online journal.)

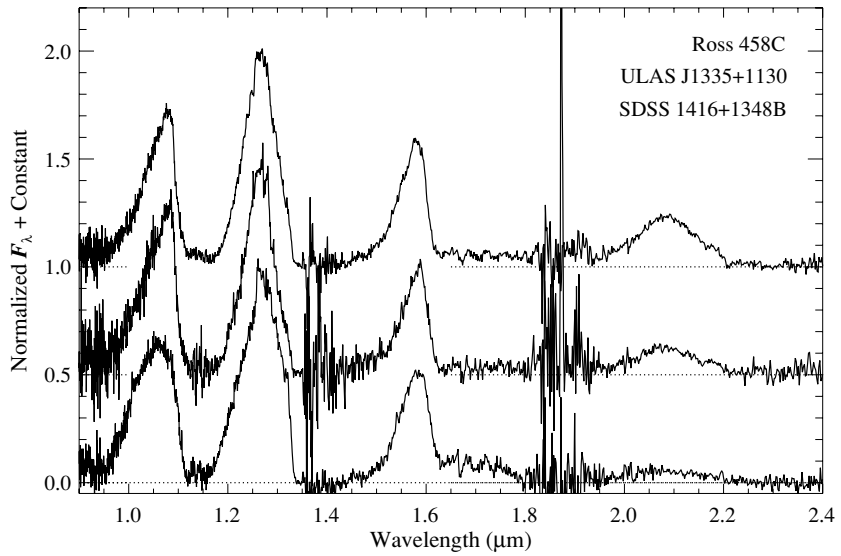

Figure 4. FIRE prism spectra of (top to bottom) Ross 458C, ULAS J1335+1130, and SDSS J1416+1348B. Data are normalized at 1.27 μm and offset by constants (dotted lines). Note the variations in the *Y*- and *K*-band flux peaks.

dwarf, we derive estimates of $\log_{10} L_{\rm bol}/L_\odot = -5.69 \pm 0.06$, $\log_{10} L_{\rm bol}/L_\odot = -5.65 \pm 0.04$, and $\log_{10} L_{\rm bol}/L_\odot = -5.55 \pm 0.05$ based on *J*-, *H*-, and *K*-band fluxes, or a weighted mean of $\log_{10} L_{\rm bol}/L_\odot = -5.62 \pm 0.03$. This luminosity is similar to that of the T8 spectral standard 2MASS J04151954−0935066 (hereafter 2MASS J0415−0935; $\log_{10} L_{\rm bol}/L_\odot = -5.67 \pm 0.02$; Saumon et al. 2007). The $T_{\rm eff}$ of Ross 458C can be inferred from its luminosity by adopting a radius from the evolutionary models of SM08. For an age of 150–800 Myr (Section 2.2), these models predict a radius of 0.12–0.13 $R_\odot$, $T_{\rm eff} = 650 \pm 25$ K, and a mass in the range 0.006–0.011 $M_\odot$. The inferred temperature is cooler than that of 2MASS J0415−0935 ($T_{\rm eff} = 750 \pm 25$ K; Saumon et al. 2007) due to the inflated radius, while the inferred mass is below the deuterium burning minimum mass limit (0.014 $M_\odot$; Chabrier & Baraffe 2000; Spiegel et al. 2010).

4. SPECTRAL MODEL FITS

4.1. Spectral Models and Method

We compared the FIRE spectra of these three T dwarfs to a suite of atmosphere models from Marley et al. (2002) and SM08, following the prescriptions detailed in Cushing et al. (2008), Burgasser et al. (2008b), and Bowler et al. (2009). The one-dimensional models include all significant gas species considered in Freedman et al. (2008) including CO_2 (cf. Yamamura et al. 2010), albeit with line lists for CH_4 and NH_3 that are known

Table 2
Spectral Indices for Observed T Dwarfs

Index	Ross 458C		ULAS J1335+1130		SDSS J1416+1348B		
	Value[a]	SpT	Value[a]	SpT	Value[a]	SpT	Ref.
H_2O–J	0.051 ± 0.002	T8.0	0.028 ± 0.003	T8.5	0.044 ± 0.003	T8.0	1
CH_4–J	0.154 ± 0.001	T8.5	0.109 ± 0.002	T9.0	0.262 ± 0.002	T7.0	1
W_J	0.272 ± 0.002	T9.0	0.253 ± 0.002	T9.0	0.360 ± 0.002	T7.0	2,3
H_2O–H	0.193 ± 0.003	T7.5	0.192 ± 0.007	T7.5	0.148 ± 0.004	T9.0	1
CH_4–H	0.112 ± 0.003	T8.0	0.068 ± 0.005	T9.0	0.192 ± 0.003	T7.0	1
NH_3–H	0.632 ± 0.004	...	0.537 ± 0.007	...	0.610 ± 0.005	...	4
CH_4–K	0.078 ± 0.005	T7.5	0.073 ± 0.013	T7.5	0.191 ± 0.032	T5.5	1
K/J	0.167 ± 0.001	...	0.130 ± 0.002	...	0.044 ± 0.001	...	1
$J - H$[b]	−0.14 ± 0.01	...	−0.34 ± 0.02	...	−0.25 ± 0.01	...	
$H - K$[b]	0.38 ± 0.02	...	0.06 ± 0.05	...	−1.02 ± 0.09	...	
$J - K$[b]	0.24 ± 0.02	...	−0.28 ± 0.04	...	−1.25 ± 0.09	...	

Notes.
[a] Values for each source were measured for 1000 realizations of the spectrum (100 realizations for spectrophotometric colors), each with a normal distribution of random values scaled by the noise spectrum added to the original fluxes. The reported values are the means and standard deviations of these measurements.
[b] Spectrophotometric colors computed according to Cushing et al. (2005).
References. (1) Burgasser et al. 2006b; (2) Warren et al. 2007; (3) Burningham et al. 2008; (4) Delorme et al. 2008.

to be incomplete (e.g., Saumon et al. 2006). Solar abundances from Lodders (2003) were assumed. Non-equilibrium chemistry of CO, CH_4, H_2O, and NH_3 (the relevant molecules influencing the near-infrared spectra of T dwarfs) by vertical transport was accounted for using an eddy diffusion parameterization, K_{zz} (Fegley & Lodders 1996; Griffith & Yelle 1999; Saumon et al. 2006; Hubeny & Burrows 2007). Equilibrium condensate formation was included in the chemistry,[17] with grain size and vertical distributions parameterized by a sedimentation rate $f_{\rm sed}$ (Ackerman & Marley 2001; Marley et al. 2002). While contemporaneous studies of late-type T dwarfs have generally ignored the opacity from condensate grains (e.g., Leggett et al. 2007, 2009; Saumon et al. 2007; Burgasser et al. 2008b), we considered two sets of SM08 models with ("cloudy") and without ("cloudless") condensate opacity included. Both sets of models use the same gas chemistry and have the same constituent abundances at any given pressure and temperature. The cloudless models assume that condensates do not contribute to the opacity (but do contribute to the gas chemistry), perhaps because they have "rained out" of the atmosphere or occupy only a small fraction of the visible surface area. The cloudy models explicitly include opacity from cloud grains. The cloudless models sampled atmospheric parameters $T_{\rm eff}$ = 500–1000 K (50 K steps); $\log g$ = 4.0–5.5 cgs (0.5 dex steps); [M/H] = −0.3, 0, and +0.3 dex relative to solar; and $K_{zz} = 0$ and 10^4 cm^2 s^{-1}. The cloudy models sampled the same parameter space with $f_{\rm sed} = 2$ and solar metallicity alone. Hereafter, we refer to sets of parameters by the notation $\mathbf{k} = (T_{\rm eff}, \log g, [{\rm M/H}], f_{\rm sed}, \log K_{zz})$, where $f_{\rm sed}$ = NC for the cloudless models. The model spectra were computed as surface fluxes (F_ν flux units), smoothed to the mean resolution of the FIRE prism data ($\lambda/\Delta\lambda = 300$) using a Gaussian kernel, and interpolated onto the same wavelength scale as the data. We also assigned physical parameters of mass, age, and radius to each spectral model, interpolating the appropriate evolutionary tracks from SM08.

The observational data (also in F_ν flux units) were scaled to their apparent UKIDSS J-band magnitudes. Simultaneous fits were made to the 0.85–1.35 μm, 1.42–1.8 μm, and 1.95–2.35 μm regions to avoid strong telluric absorption. For each data-model comparison, the goodness-of-fit statistic $G_{\mathbf{k}}$ (Cushing et al. 2008) was calculated following the same weighting scheme employed in that study, with each pixel weighted by its breadth in wavelength space ($w_j \propto \Delta\lambda_j$). Model surface fluxes were scaled by the factor $C_{\mathbf{k}} \equiv (R/d)^2$ which minimizes $G_{\mathbf{k}}$ (Equation (2) in Cushing et al. 2008), where R is the radius of the brown dwarf and d is its distance from the Earth. As in Burgasser et al. (2008b), we generated distributions of the fit parameters by weighting each model's contribution according to the F-distribution probability distribution function (PDF):

$$W_i \propto 1 - F(G_{\mathbf{k_i}}/\min(G_{\mathbf{k}}) \mid \nu_{\rm eff}, \nu_{\rm eff}). \quad (1)$$

Here, $G_{\mathbf{k_i}}/\min(G_{\mathbf{k}})$ is the ratio of goodness-of-fit (effectively a ratio of chi-square residuals) between the best-fit model and the ith model, and $F(x|\nu_{\rm eff}, \nu_{\rm eff})$ is the F-distribution PDF for effective degrees of freedom:

$$\nu_{\rm eff} \equiv \left(\frac{1}{\max(\{w\})} \sum_{j=1}^{N} w_j \right) - 1. \quad (2)$$

The sum is over all pixels included in the fit (see Burgasser et al. 2010a). The F-distribution provides a more robust assessment of the equivalence of different model fits than the exponential weighting employed in Burgasser et al. (2008b) and Burgasser et al. (2010b). Parameter means and one-sided standard deviations were separately computed as

$$\langle \mathbf{k} \rangle \equiv \frac{\sum_i W_i \mathbf{k}_i}{\sum_i W_i} \quad (3)$$

and

$$\sigma^2_{\mathbf{k}_\pm} = \frac{\sum_{i_\pm} W_i (\mathbf{k}_i - \langle \mathbf{k} \rangle)^2}{\sum_i W_i}. \quad (4)$$

[17] The chemical equilibrium calculation accounts for all important condensed species (Lodders & Fegley 2006; Visscher et al. 2010). For the cloud opacity, we included only silicates, iron, and Al_2O_3 (alumina or corundum). Other condensates are expected to form above the silicate cloud at low effective temperature, but of these only Na_2S is likely to have any significant column opacity (Marley 2000). In a future work, we will consider the possible contribution of this species.

Table 3
Model-fit Parameters for Observed T Dwarfs

Parameter	Best Fit (Cloudless)	Mean (Cloudless)	Best Fit (Cloudy)	Mean (Cloudy)	Prior Value	Ref.
			Ross 458C (T8)			
G_k	71.8	...	51.3	...	...	
d/R (pc/$R_{\rm Jup}$)	11.5	13.4 ± 1.9	7.9	7.5 ± 0.6	...	
$T_{\rm eff}$ (K)	700	760^{+70}_{-45}	650	635^{+25}_{-35}	...	
log g (cm s^{-2})	4.0	$4.2^{+0.3}_{-0.2}$	4.0	$\approx$4.0	...	
[M/H] (dex)	+0.3	$\approx$+0.3	0[a]	0[a]	+0.2...+0.3	1
K_{zz} (cm^2 s^{-1})	10^4	...	0	...	...	
Mass ($M_\odot$)	0.006	$0.010^{+0.006}_{-0.004}$	0.006	$\lesssim$0.006	0.006–0.011[b]	1
Age (Gyr)	0.08	$0.3^{+0.5}_{-0.2}$	0.13	$0.14^{+0.03}_{-0.01}$	0.4–0.8	1
					0.4-2	2
R ($R_{\rm Jup}$)	1.22	$1.16^{+0.07}_{-0.09}$	1.25	$\approx$1.24	...	
d (pc)	14.1	15.6 ± 2.5	9.8	9.4 ± 0.7	11.7 ± 0.2	3
			ULAS J1335+1130 (T9)			
G_k	22.7	...	21.0	...	...	
d/R (pc/$R_{\rm Jup}$)	20.9	20.2 ± 2.4	12.0	11.8 ± 0.8	...	
$T_{\rm eff}$ (K)	700	700^{+30}_{-50}	600	595^{+25}_{-45}	500–600	4,5
log g (cm s^{-2})	5.0	4.7 ± 0.4	4.0	$\approx$4.0	4.0–4.5	4,5
[M/H] (dex)	+0.3	$+0.23^{+0.07}_{-0.23}$	0[a]	0[a]	0...+0.3	5
K_{zz} (cm^2 s^{-1})	10^4	...	0	...	...	
Mass ($M_\odot$)	0.031	0.021 ± 0.011	0.006	0.005–0.013	0.014–0.030	4
					0.005–0.019	5
Age (Gyr)	3.3	$2.0^{+2.3}_{-1.6}$	0.17	$0.18^{+0.23}_{-0.01}$	0.6–5.3	4
					0.01–2	5
R ($R_{\rm Jup}$)	0.90	$1.01^{+0.13}_{-0.12}$	1.23	$\approx$1.23	1.07–1.17	5
d (pc)	18.7	20.5 ± 3.6	14.7	14.4 ± 1.1	8–12	4,5
			SDSS J1416+1348B (T7.5p)			
G_k	22.3	...	21.0	...	...	
d/R (pc/$R_{\rm Jup}$)	15.0	13.2 ± 3.6	15.1	13.2 ± 4.0	12.8 ± 3.0	6
$T_{\rm eff}$ (K)	700	685^{+55}_{-65}	600	595^{+25}_{-45}	650 ± 60	6
					500	7
log g (cm s^{-2})	5.5	5.2 ± 0.3	5.5	$\approx$5.5	5.2 ± 0.4	6,7
[M/H] (dex)	0.0	$-0.17^{+0.17}_{-0.13}$	0[a]	0[a]	−0.3	6,7
K_{zz} (cm^2 s^{-1})	10^4	...	0	...	10^4	6,7
Mass ($M_\odot$)	0.052	$0.041^{+0.011}_{-0.010}$	0.036	$0.035^{+0.001}_{-0.003}$	0.021–0.045	6
					0.029–0.038	7
Age (Gyr)	12	8 ± 4	12	6–12	2–10	6,7
R ($R_{\rm Jup}$)	0.78	0.84 ± 0.06	0.86	$\approx$0.86	$0.83^{+0.14}_{-0.10}$	6
d (pc)	11.8	11.1 ± 3.2	13.0	11.4 ± 3.4	7.9 ± 1.7	8

Notes.
[a] Solar metallicity is assumed for all cloudy models.
[b] Mass estimate based on the luminosity and estimated age of Ross 458C, and the cloudy evolutionary models of SM08.
References. (1) This paper; (2) Goldman et al. 2010; (3) van Leeuwen 2007; (4) Burningham et al. 2008; (5) Leggett et al. 2009; (6) Burgasser et al. 2010b; (7) Burningham et al. 2010; (8) Scholz 2010b.

The first sum was performed over all models and the second restricted to those models whose parameter values are above (+) or below (−) the weighted mean $\langle \mathbf{k} \rangle$.

We examined several variations in our fitting method to assess internal systematic effects. Modest changes to the spectral regions that contributed to computing $G_{\mathbf{k}}$ made little difference to the overall best fit. For example, including the telluric regions in the fits, or expanding the lower and upper ends of the spectral range used, resulted in changes of less than 10 K and 0.1 dex in the mean $T_{\rm eff}$ or log g values for all three sources. Only by excluding whole spectral regions—such as the individual *YJHK*-band flux peaks—did inferred $T_{\rm eff}$ and log g values change significantly, by up to 100 K and 0.5 dex (similar to band-to-band variations reported in Cushing et al. 2008). Variations in the pixel weighting scheme also had negligible effect. Weighting all pixels equally gave identical parameters (to within 10 K and 0.1 dex in $T_{\rm eff}$ and log g) as weighting by pixel bandpass. Finally, using the exponential parameter weighting employed in Burgasser et al. (2010b), $W_i \propto e^{-0.5 G_{\mathbf{ki}}}$, also produced negligible changes in the inferred parameters and their uncertainties. We therefore assume systematic uncertainties of 20 K in $T_{\rm eff}$ and 0.2 dex in log g, although we cannot rule out larger systematic *biases* based on the accuracy of the models.

4.2. Results

Table 3 summarizes the inferred parameters for each source, with results for the cloudless and cloudy models reported separately. Figures 5–7 show the best-fit models to the individual spectra, while Figures 8–10 show the parameter distributions.

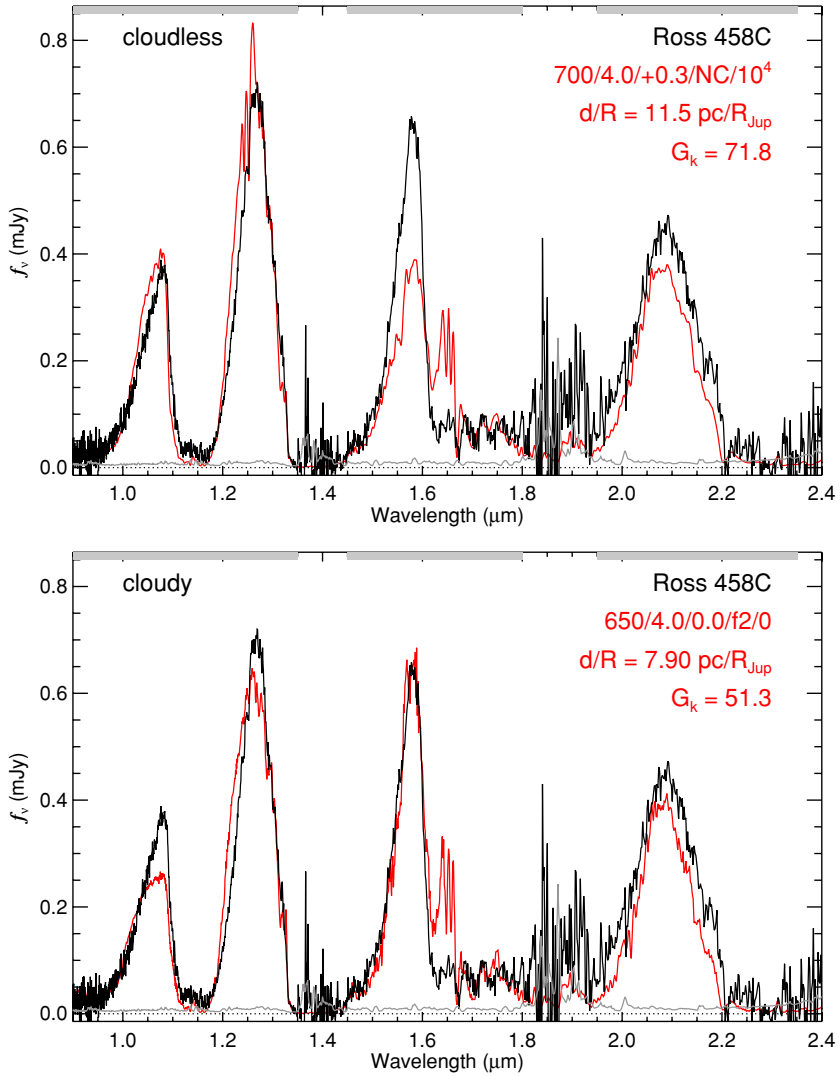

Figure 5. Best-fit cloudless (top) and cloudy (bottom) model fits (red lines) to the observed spectrum for Ross 458C (black lines). Observed data are scaled to the apparent UKIDSS *J*-band magnitude of the source, while the model is scaled to minimize G_k (indicated, along with d/R flux scaling factor). The noise spectrum for Ross 458C is shown by the gray lines, and fit regions indicated by the shaded boxes at the top of each panel.

(A color version of this figure is available in the online journal.)

It is first worth noting the quality of the fits. For both cloudless and cloudy models, deviations are seen in regions of strong CH_4 absorption, particularly in the 1.6–1.7 μm region for Ross 458C and ULAS J1335+1130 and the wings of the 1.27 μm *J*-band peak for SDSS J1416+1348B. As noted previously, these discrepancies are likely the result of incomplete CH_4 opacities (Saumon et al. 2006). However, there are also differences between the cloudless and cloudy model fits, notably in the relative *YJH* peak fluxes of Ross 458C and ULAS J1335+1130. In the cloudless model fits of these sources, the *H*-band peak appears to be suppressed relative to *J*, while the *Y*-band peak appears suppressed in the cloudy model fits. These differences are less pronounced in fits to SDSS J1416+1348B. The cloudless models also exhibit excessively strong K I lines at 1.24–1.25 μm, while these lines in the cloudy models are more consistent with the data. For both models, the 2.1 μm *K*-band peak is reasonably well reproduced for all three sources (see also Cushing et al. 2008). Nevertheless, it appears that the cloudy models provide better matches to the data than the cloudless ones.

Quantitative differences between the cloudless and cloudy model fits are also seen. For Ross 458C (Figures 5 and 8), the cloudy model provides a statistically superior fit to the data, significant at the 99.99% confidence level based on the *F*-test PDF. The cloudy model also predicts a significantly cooler temperature than the cloudless case, $T_{\rm eff} = 635^{+25}_{-30}$ K versus $T_{\rm eff} = 760^{+70}_{-45}$ K. The former value is consistent with the luminosity-based $T_{\rm eff}$ determined in Section 3.5, while the latter is consistent with a "normal" T8 field dwarf like 2MASS J0415−0935 (e.g., Golimowski et al. 2004; Stephens et al. 2009). Inferred surface gravities are comparable for the two models, favoring $\log g \approx 4.0$ cgs, while the cloudless models indicate a metal-rich atmosphere ([M/H] $\approx +0.3$). These parameters are consistent with the youth and metallicity of the Ross 458 system, as the mean cloudless and cloudy model ages are $0.3^{+0.5}_{-0.2}$ Gyr and $0.14^{+0.03}_{-0.01}$ Gyr, respectively. Both models also predict a very low mass for Ross 458C, $M = 0.010^{+0.006}_{-0.004}\,M_\odot$, and M $\lesssim$0.006 $M_\odot$, again at or below the deuterium burning mass limit. There is a modest difference between whether vertical mixing is slightly favored (cloudless models) or not (cloudy

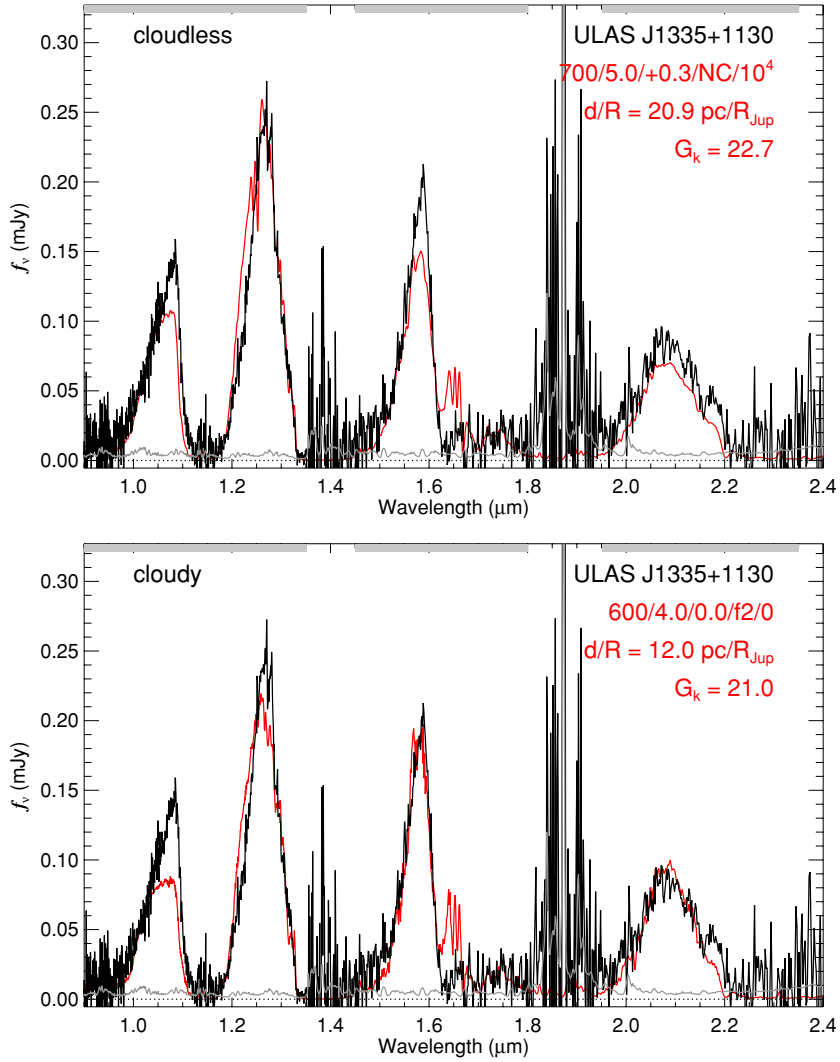

Figure 6. Same as Figure 5 for ULAS J1335+1130.
(A color version of this figure is available in the online journal.)

models), but it is not statistically significant. The cloudless and cloudy models predict distinct distances of 15.6 ± 2.5 pc and 9.4 ± 0.7 pc, respectively, based on the optimal model scaling. These differ by 2.6σ and are 1.8σ higher and 2.4σ lower than the parallactic distance of the Ross 458 system, although the latter is off by only 11%.

For ULAS J1335+1130 (Figures 6 and 9), the best-fit cloudy model also has a smaller G_k value than the best-fit cloudless one, although the statistical significance is reduced (84% confidence level). Again, the cloudy models predict a significantly lower effective temperature than the cloudless models ($T_{\rm eff} = 595^{+25}_{-45}$ K versus $T_{\rm eff} = 700^{+30}_{-50}$ K). The former is consistent with the previously reported values by Burningham et al. (2008, 550–600 K) and Leggett et al. (2009, 500–550 K). The cloudy models also indicate a lower surface gravity ($\log g \approx 4.0$ cgs versus $\log g = 4.7 \pm 0.4$ cgs), while differences in vertical mixing are statistically unconstrained. Like Ross 458C, the cloudless models converge on a supersolar metallicity for ULAS J1335+1130, [M/H] $= +0.23^{+0.07}_{-0.23}$. The differing parameters between the cloudless and cloudy models translate into marginally overlapping ages ($2.0^{+2.3}_{-1.6}$ Gyr versus $0.18^{+0.23}_{-0.01}$ Gyr) and masses (0.010–0.032 $M_\odot$ versus 0.005–0.013 $M_\odot$), and distinct distances (20.5 ± 3.6 pc versus 14.4 ± 1.1 pc, a 1.6σ discrepancy).

Finally, for SDSS J1416+1348B (Figures 7 and 10), we again find that the best-fit cloudy model is marginally better than the best-fit cloudless one, albeit at even lower statistical significance (confidence level of 77%) reflecting the similarity in the near-infrared SEDs of these models. Nevertheless, the inferred temperatures are marginally distinct, with the cloudy models again indicating a cooler temperature ($T_{\rm eff} = 595^{+25}_{-45}$ K versus $T_{\rm eff} = 685^{+55}_{-65}$ K). Unlike Ross 458C and ULAS J1335+1130, the inferred surface gravity of this source is considerably higher ($\log g = 5.2 \pm 0.3$ cgs cloudless; $\log g \approx 5.5$ cgs cloudy), while the cloudless model indicates a subsolar metallicity ([M/H] $= -0.17^{+0.17}_{-0.13}$). As discussed in Burningham et al. (2010) and Burgasser et al. (2010b), high surface gravity and/or subsolar metallicity are required to produce both the suppressed K-band peak and broadened Y-band peak observed in the spectrum of this source. Vertical mixing is again poorly constrained. The inferred atmospheric parameters of SDSS J1416+1348B indicate a brown dwarf that is older (4–12 Gyr) and more massive (0.03–0.05 $M_\odot$) than the other two sources, consistent with prior analyses. Surprisingly, the cloudless and cloudy models converge on a common distance of 11 ± 3 pc, larger than but formally consistent with the preliminary parallax measurement of Scholz (2010b, 7.9 ± 1.7 pc).

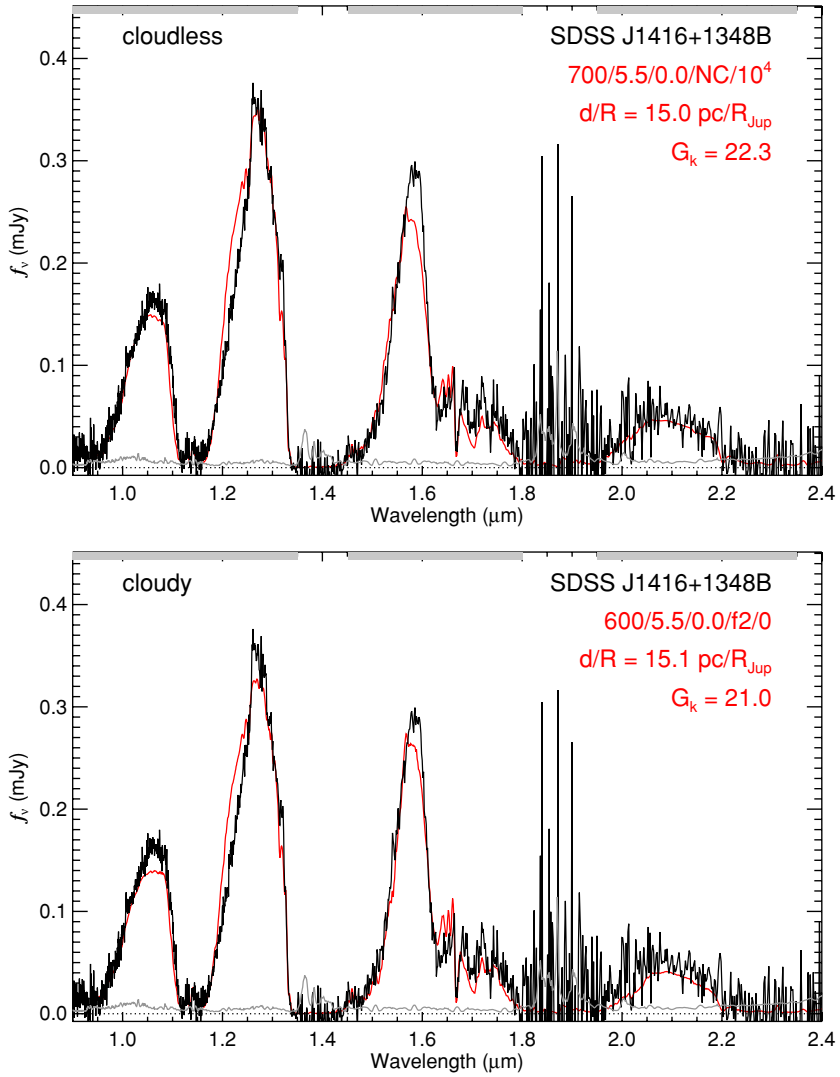

Figure 7. Same as Figure 5 for SDSS J1416+1348B.
(A color version of this figure is available in the online journal.)

5. DISCUSSION

5.1. Clouds in Young, Cold, and Metal-rich T Dwarfs

The above analysis illustrates how condensate opacity, when included in spectral models, can have a profound effect on the near-infrared SEDs and inferred $T_{\rm eff}$s of the coldest T dwarfs. More importantly, the inclusion of condensate opacity provides a statistically significant improvement in fits to the near-infrared spectrum of Ross 458C, and marginally so for ULAS J1335+1130 and SDSS J1416+1348B. This is not the first indication of condensates being present in T dwarf atmospheres. Early-type T dwarfs exhibit evidence of waning cloud opacity (Marley et al. 2002; Cushing et al. 2008; Leggett et al. 2008), and SM08 have shown that T dwarf models produce excessively blue near-infrared colors without the inclusion of condensate extinction. Nevertheless, several theoretical studies have concluded that condensate clouds play little or no role in shaping the near-infrared spectra of brown dwarfs cooler than ≈1000 K, as they reside below the visible photosphere (e.g., Allard et al. 2001; Burrows et al. 2006). Instead, we find that clouds are *essential* for reproducing the near-infrared SED of the $T_{\rm eff} \approx$ 650 K T dwarf Ross 458C, and to a lesser degree the $T_{\rm eff} \approx$ 600 K T dwarfs ULAS J1335+1130 and SDSS J1416+1348B.

The importance of clouds in these two sources is likely related to their youth and associated low surface gravities. Among the L dwarfs, a correlation between low surface gravity and thick clouds has been noted by Cushing et al. (2008) and Stephens et al. (2009) based on broadband spectral model fits, and by Metchev & Hillenbrand (2006) and Dupuy et al. (2009b) based on the delayed disruption of clouds at the L dwarf/T dwarf transition. There is also evidence that this correlation continues into the T dwarf regime, based on cloudy model fits to broadband spectral data for the low-gravity T5.5 dwarf SDSSp J111010.01+011613.1 (Stephens et al. 2009). Finally, the 9–11 μm silicate grain feature has also been shown to be more pronounced in L dwarfs with unusually red $J - K$ colors (Burgasser et al. 2008a; Looper et al. 2008), sources whose kinematics reflect youth and low surface gravities (Faherty et al. 2009; Schmidt et al. 2010).

Atmospheric models show that two complementary effects can drive the persistence of clouds in low-gravity, low-temperature brown dwarf atmospheres. First, the column of atmosphere above a given pressure level is deeper in a lower

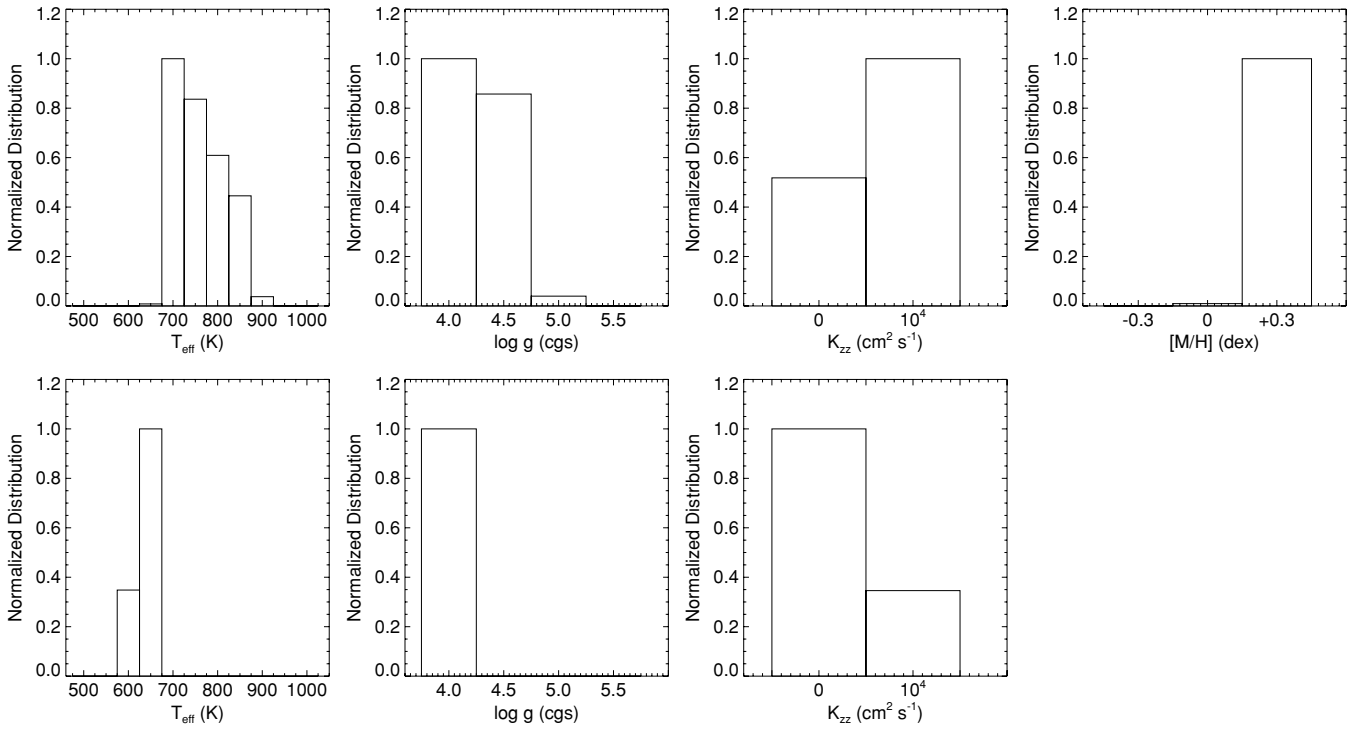

Figure 8. Parameter distributions for cloudless (top) and cloudy (bottom) model fits of Ross 458C, based on the parameter weighting scheme described in the text. From left to right, distributions in $T_{\rm eff}$, log g, and K_{zz} are shown. For the cloudless models, the distribution in [M/H] values is also shown.

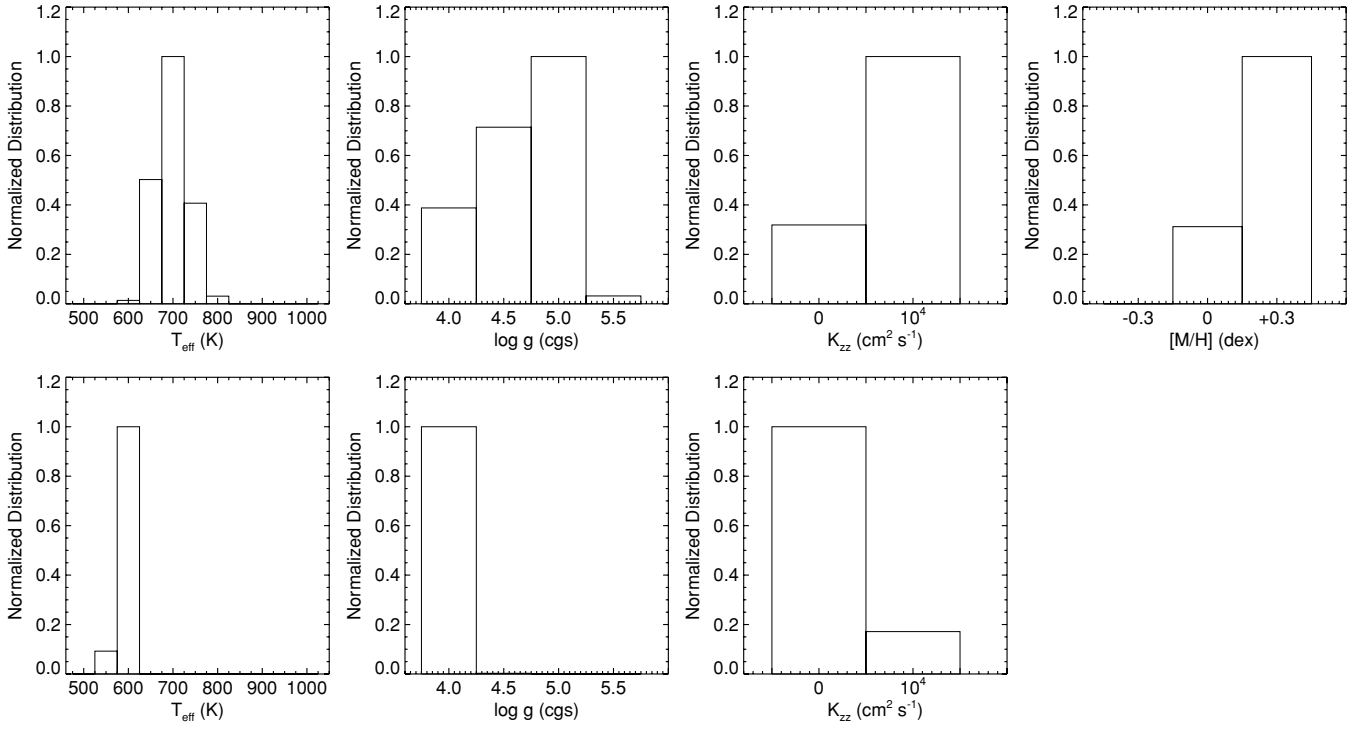

Figure 9. Same as Figure 8 for ULAS J1335+1130.

gravity dwarf, and as a consequence the atmosphere is everywhere warmer at a fixed $T_{\rm eff}$. This implies that silicate clouds lie higher in these atmospheres, providing a larger column depth of extinction in regions of minimum molecular gas opacity. Second, cloud models from Ackerman & Marley (2001) and Helling et al. (2008) both predict that mean cloud particle sizes are larger in lower gravity atmospheres. In a $T_{\rm eff} = 650$ K SM08 model, for example, the mean particle radius is roughly 10 times larger for log $g = 4.5$ as compared to log $g = 5.5$. The sub-micron particles found in higher gravity models contribute little opacity in the near-infrared because of Mie-scattering effects, rendering the deep silicate cloud less visible. Clouds in lower gravity dwarfs are therefore more visible and scatter more efficiently than those in their older and more massive

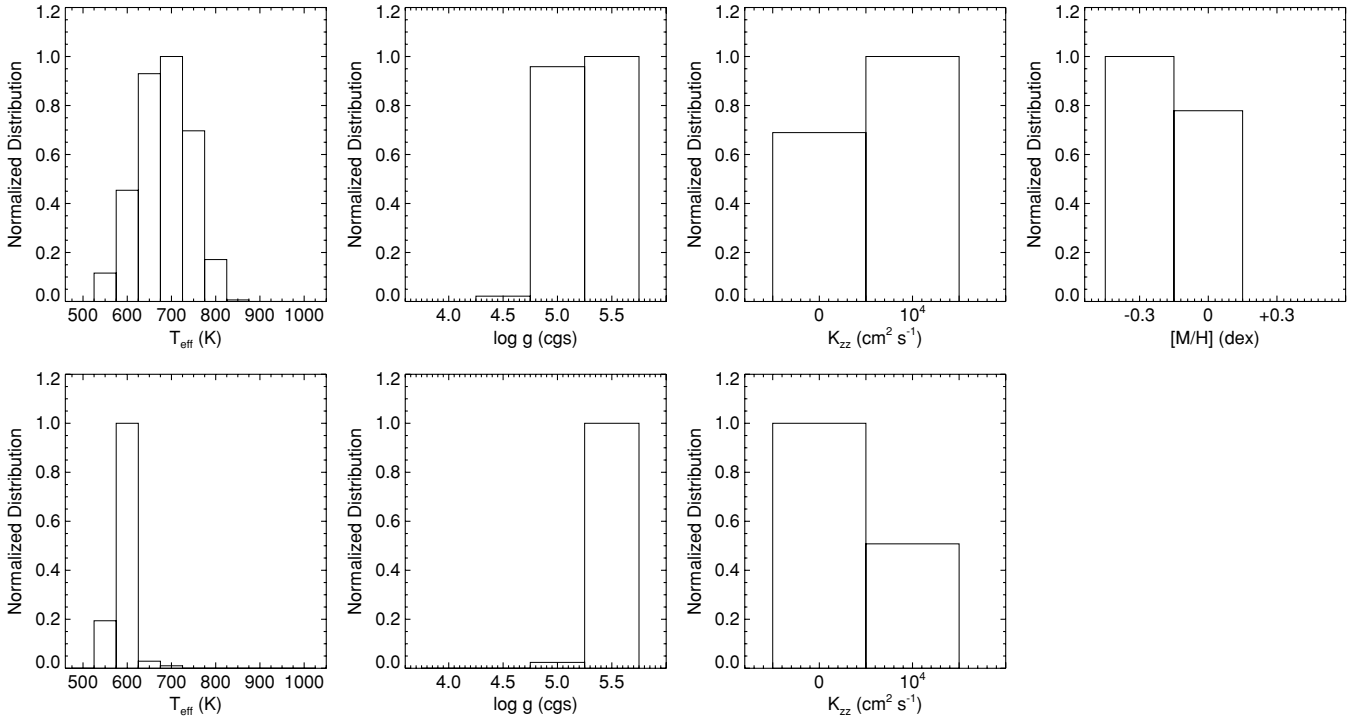

Figure 10. Same as Figure 8 for SDSS J1416+1348B.

counterparts. This interpretation explains why cloudless models have so far provided adequate fits to the spectra of $\log g \gtrsim 5$ T dwarfs (e.g., Geballe et al. 2001; Saumon et al. 2007; Burgasser et al. 2008b), including SDSS J1416+1348B.

Metallicity is another factor to consider. Cloud formation appears to be inhibited in metal-poor L subdwarfs, as exemplified by the retention of Ca, Ti, and TiO gas to cooler $T_{\rm eff}$s in these objects (Burgasser et al. 2003, 2007; Gizis & Harvin 2006). Similarly, unusually blue L dwarfs—including the brighter companion of SDSS J1416+1348B—appear to have slightly metal-poor atmospheres with unusually thin clouds (Burgasser et al. 2008a; Cushing et al. 2010) or fractured cloud layers (Marley et al. 2010). It is not unreasonable to speculate that supersolar metallicity dwarfs may have thicker clouds (Looper et al. 2008), yet theoretical predictions are mixed. SM08 have shown that warmer cloudy models ($T_{\rm eff} \geqslant 1300$ K) appear "cloudier" (redder) for supersolar metallicities. However, chemical equilibrium calculations by Visscher et al. (2010) find that $MgSiO_3$ (enstatite) condenses at warmer temperatures in higher metallicity atmospheres, leading to a deeper cloud that may be buried by gas opacity in cooler brown dwarfs. Atmospheric model calculations by Witte et al. (2009) find that grain size and cloud optical depth do not change appreciably between [M/H] = 0 and +0.5 for low-temperature brown dwarfs, although the clouds themselves expand into lower pressure regions of the atmosphere and may have a greater effect at wavelengths corresponding to minimum gas opacity. Metallicity effects on cloud formation and cloud properties in cool T dwarf atmospheres clearly remains an area of further theoretical exploration.

In summary, the unexpected presence of condensate absorption in the spectrum of Ross 458C (and possibly ULAS J1335+1130) can be attributed to its low surface gravity, and possibly its supersolar metallicity. This hypothesis follows similar trends observed in the L dwarfs. It also explains why clouds had not previously been needed in model fits of high surface gravity T dwarfs. The importance of clouds in shaping low-gravity T dwarf spectra should nevertheless be a consideration in the characterization of planetary-mass brown dwarf candidates in local young clusters (e.g., Zapatero Osorio et al. 2002; Casewell et al. 2007; Burgess et al. 2009; Marsh et al. 2010) and low-mass exoplanets recently imaged around nearby young stars (e.g., Kalas et al. 2008; Marois et al. 2008; Janson et al. 2010; Lagrange et al. 2010).

5.2. Clouds and the Convergence of Near-infrared and Mid-infrared T Dwarf Temperature Scales

Spitzer has enabled detailed studies of cold T dwarfs in the mid-infrared, where the majority of the SED emerges (Leggett et al. 2010). Model fits to mid-infrared spectral data have proven particularly robust, with agreement in continuum fluxes and prominent H_2O, CH_4, and NH_3 bands (e.g., Saumon et al. 2007; Burgasser et al. 2008b; Leggett et al. 2009). However, there have been indications that temperatures inferred from near- and mid-infrared analyses can differ significantly. A case in point is SDSS J1416+1348B. Burgasser et al. (2010b) inferred $T_{\rm eff} = 650 \pm 60$ K for this source from near-infrared cloudless spectral model fits, similar to the cloudless results presented here. Burningham et al. (2010) inferred $T_{\rm eff} \approx 500$ K based on the extreme $H - [4.5]$ color of this source (Warren et al. 2007; Leggett et al. 2010). We find that the inclusion of cloud opacity in the near-infrared modeling of this source brings inferred $T_{\rm eff}$s closer to mid-infrared results, despite having minimal effect on the shape of its spectrum. Even better convergence is seen for ULAS J1335+1130, as our near-infrared cloudy model temperature is fully consistent with estimates based on $H - [4.5]$ color (Burningham et al. 2008) and near- to mid-infrared spectral model fits (Leggett et al. 2009). For Ross 458C, the cloudy model temperature is consistent with that inferred from evolutionary models based on the age and luminosity of the source (Section 3.5).

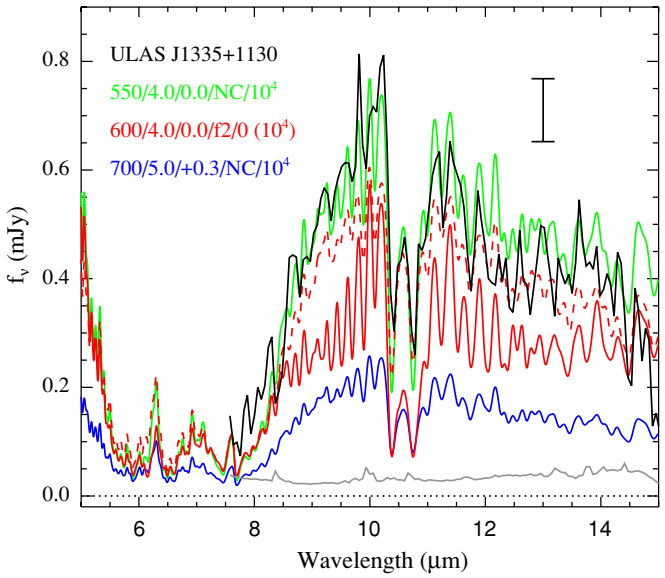

Figure 11. *Spitzer*/IRS spectrum of ULAS J1335+1130 from Leggett et al. (2009, black line, noise spectrum in gray), scaled to its apparent 8.0 μm magnitude (Burningham et al. 2008), compared to best-fit cloudless (blue line) and cloudy (solid red line) models from our near-infrared analysis, and the best-fit cloudless model from the near- and mid-infrared analysis of Leggett et al. (2009, green line). Model surface fluxes have been smoothed to the resolution of the IRS data ($\lambda/\Delta\lambda \approx 100$) using a Gaussian kernel and scaled according to their respective best-fit distances and radii. The best-fit cloudy model to the near-infrared data with $K_{zz} = 10^4$ cm^2 s^{-1} is also shown (dashed red line). Observational uncertainty in flux at 10 μm is indicated by the error bar.

(A color version of this figure is available in the online journal.)

Prior mid-infrared analyses have been based on cloudless model fits, however, so does the inclusion of clouds affect these results? To explore this question, Figure 11 compares the observed mid-infrared spectrum of ULAS J1335+1130 obtained with the *Spitzer* Infrared Spectrograph (IRS; Houck et al. 2004; Leggett et al. 2009) to three SM08 models: two sampling the best-fit parameters from our near-infrared cloudless and cloudy model fits and one sampling the cloudless model fit parameters from Leggett et al. (2009).[18] The first two models are scaled according to the near-infrared normalizations from our analysis, while the Leggett et al. model is scaled to the best-fit radius and distance derived in that study. The 600 K cloudy model comes much closer to reproducing the pseudo-continuum flux of the observed data than the 700 K cloudless model, but is still underluminous and predicts excessively strong NH_3 absorption in the 9–13 μm region. This is not a cloud effect, however, but the absence of vertical mixing in the best-fit cloudy model. Vertical mixing reduces NH_3 photospheric abundances through non-equilibrium chemistry, but has little impact on the near-infrared spectrum for $T_{\rm eff} \lesssim 1000$ K (Griffith & Yelle 1999; Saumon et al. 2006). This is confirmed in our spectral modeling, as the presence or absence of vertical mixing is statistically ambiguous (Figures 8–10). It has a profound effect on mid-infrared spectra, however, as the $T_{\rm eff} = 600$ K, $\log g = 4.0$, and $K_{zz} = 10^4$ cm^2 s^{-1} cloudy model is a good match to data for ULAS J1335+1130 (i.e., consistent within the observational uncertainties). As such, the inclusion of cloud opacity does not appear to modify mid-infrared analyses for the coldest T dwarfs.

[18] Leggett et al. (2009) used $K_{zz} = 10^6$ cm^2 s^{-1} in their best-fit models whereas we use $K_{zz} = 10^4$ cm^2 s^{-1} in Figure 11. The difference between these models is negligible.

Convergence between near-infrared and mid-infrared spectral model fit parameters and temperature scales for cold T dwarfs is important for both near- and long-term study of these objects. With *Spitzer* now depleted of cryogen, our ability to obtain mid-infrared spectroscopy for faint brown dwarfs is restricted pending deployment of the *James Webb Space Telescope* (*JWST*) Mid-Infrared Instrument (MIRI; Wright et al. 2008) later this decade. In addition, characterization of several dozens of cold brown dwarf discoveries expected from UKIDSS, the Canada–France–Hawaii Telescope Legacy Survey (CFHTLS; Delorme et al. 2008), the Wide Field Infrared Explorer (WISE; Liu et al. 2008), and the Visible and Infrared Survey Telescope for Astronomy (VISTA; McPherson et al. 2006) cannot rely on space-based spectroscopy. Accurate reproduction of ground-based near-infrared spectroscopy, facilitated by sensitive instruments such as FIRE, will be necessary to study the physical characteristics and demographics of these intrinsically faint sources.

5.3. Is Ross 458C a Planet?

Finally, we consider whether the properties of Ross 458C qualify it as a "planet" (Basri & Brown 2006; Soter 2006; Marchi 2007). In terms of present-day characteristics, the planet moniker appears appropriate. Ross 458C is gravitationally bound to stellar (hydrogen-fusing) companions and itself appears to have a mass below which no fusion is expected. Its relative mass is roughly 1:50 compared to its companions. Its surface temperature is well below those of several well-studied, so-called planets; e.g., AB Pic b (2000^{+100}_{-300} K; Bonnefoy et al. 2010), 1RXS J160929.1−210524 b (1800 ± 200 K; Lafrenière et al. 2010), 2MASS 1207−3932b (1600 ± 100 K; Mohanty et al. 2007), and HR 8799b (1300–1700 K; Bowler et al. 2010). Evidence of clouds also lends Ross 458C a decidedly planetary-like character.

However, cosmogony seems to indicate otherwise. Ross 458C's 1100 AU projected separation makes it highly unlikely to have formed according to the "standard" model; i.e., the accumulation of gas and dust in a circumstellar (perhaps in this case circumbinary) disk (Pollack et al. 1996). Indeed, if Ross 458C is a planet, it has the widest and longest (∼50,000 yr) planetary orbit known, 2–4 times wider than AB Pic b ($M \approx 0.011\,M_\odot$, $a \approx 260$ AU; Chauvin et al. 2005; Bonnefoy et al. 2010), 1RXS J160929.1−210524 ($M \approx 0.008\,M_\odot$, $a \approx 330$ AU; Lafrenière et al. 2008, 2010), CT Cha b ($M = 0.016 \pm 0.006$ AU, $a \approx 440$ AU; Schmidt et al. 2008), and UScoCTIO 106b ($M = 0.013^{+0.002}_{-0.008}$, $a \approx 670$ AU; Béjar et al. 2008). Can planets form at these separations? Some disk fragmentation simulations have been able to produce very wide (>1000 AU) substellar companions, albeit with extreme initial conditions (e.g., $M_{\rm disk}/M_* \approx 1$; Stamatellos & Whitworth 2009; Vorobyov & Basu 2010; see also Boss 2006). Planet–planet interactions have been shown to scatter sources out to orbits 100–1000 AU in size, although they are exceedingly rare (<1%) and short lived in simulations (e.g., Dodson-Robinson et al. 2009; Veras et al. 2009). The triple nature of Ross 458 may provide an angular momentum sink for such a scenario, allowing a planet to be scattered out without being ejected (Holman & Wiegert 1999; Nelson 2003; Pierens & Nelson 2008). All of these scenarios require dramatic—and highly fortuitous—dynamic interactions to send a planet formed in the region of a circumstellar/circumbinary disk to an orbital radius 100 times wider than Jupiter's. Of course, a simpler alternative may be that Ross 458

formed as a "normal" hierarchical triple star system, albeit one with very low mass components.

Ross 458C therefore stands as a benchmark not just for studies of low-temperature, planetary-like atmospheres, but for the definition of the word planet in general. Better characterization of the age of this system and the orbital and physical properties of its components will ultimately help us address what parameter space defines a planet, and whether "well-defined boundaries, empirical verifiability, or logical consistency. . . [can] overcome gut feelings" (Basri & Brown 2006).

6. SUMMARY

We have obtained FIRE near-infrared spectra of the faint companion Ross 458C and the late-type field T dwarfs ULAS J1335+1130 and SDSS J1416+1348B. Data for the first source confirm its substellar nature and identify it as a T8 dwarf, with an inferred $\log_{10} L_{\rm bol}/L_{\odot} = -5.62 \pm 0.03$ and $T_{\rm eff} = 650 \pm 25$ K based on empirical bolometric corrections and evolutionary models. These data also show a pronounced *K*-band peak and relatively red $J - K$ spectrophotometric colors, indicative of supersolar metallicity and youth that coincide with the properties of the Ross 458 system (age = 150–800 Myr, [Fe/H] = +0.2 to +0.3). Fits of the data to synthetic spectra from SM08 confirm these secondary parameters, albeit with discrepant effective temperatures and distances depending on the presence or absence of condensate opacity. In fact, cloudy models provide significantly better fits to the near-infrared spectrum of Ross 458C and closer agreement with its parallax distance, while also providing marginally better fits to data for ULAS J1335+1130 and SDSS J1416+1348B. The fact that cloud opacity effects are more pronounced in the spectra of Ross 458C and ULAS J1335+1130 indicates that clouds are particularly relevant for shaping the spectra of young, low-gravity brown dwarfs, and/or those with supersolar metallicities, following trends seen in the warmer L dwarfs.

Despite the improvement, model fits to brown dwarf spectra remain a work in progress. The cloudy models "overcorrect" *Y*- and *J*-band fluxes and underestimate absolute fluxes in the case of Ross 458C. Both shortcomings suggest that thinner clouds (e.g., $f_{\rm sed} = 3$ or 4) may be needed to accurately account for condensate extinction, in line with values inferred for L/T transition objects (Cushing et al. 2008; Stephens et al. 2009). Furthermore, the limited sample examined here may not be representative of the greater population of low-temperature, low-surface-gravity T dwarfs. A comprehensive modeling effort can more fully explore the properties of clouds in these objects, while accurate parallax measurements would provide the necessary empirical constraints on surface fluxes. Nevertheless, our results indicate that by including condensate opacity in T dwarf spectral models, more accurate determinations of the physical parameters of cold brown dwarfs and exoplanets are possible with near-infrared spectroscopy alone.

The authors acknowledge the efforts of the Las Campanas Observatory staff in helping us bring FIRE to the first light and science operations. Specifically, we thank Frank Peréz, Alan Uomoto, Mark Phillips, Dave Osip, and Povilas Palunas for their assistance during commissioning. We also thank our telescope operators Jorge Araya, Mauricio Martinez, and Hernán Nuñez for their assistance during the observations. We acknowledge helpful comments from G. Bjorn, B. Bowler, J. Faherty, J. Gizis, D. Looper, and R.-D. Scholz and thank our referee C. Visscher for his prompt and helpful review of our original manuscript. The authors also thank B. Burningham and S. Leggett for providing their spectral data of ULAS J1335+1130, and J. D. Kirkpatrick for providing his spectrum of Ross 458AB used in the analysis. Support for the modeling work of D.S. was provided by NASA through the *Spitzer* Science Center. This research has benefited from the M, L, and T dwarf compendium housed at DwarfArchives.org and maintained by Chris Gelino, Davy Kirkpatrick, and Adam Burgasser.

Facility: Magellan:Baade (FIRE)

REFERENCES

Ackerman, A. S., & Marley, M. S. 2001, ApJ, 556, 872
Allard, F., Hauschildt, P. H., Alexander, D. R., Tamanai, A., & Schweitzer, A. 2001, ApJ, 556, 357
Allard, N. F., Allard, F., Hauschildt, P. H., Kielkopf, J. F., & Machin, L. 2003, A&A, 411, L473
Antoja, T., Figueras, F., Fernández, D., & Torra, J. 2008, A&A, 490, 135
Barnes, S. A. 2003, ApJ, 586, 464
Basri, G., & Brown, M. E. 2006, Annu. Rev. Earth Planet. Sci., 34, 193
Béjar, V. J. S., Zapatero Osorio, M. R., Pérez-Garrido, A., Álvarez, C., Martín, E. L., Rebolo, R., Villó-Pérez, I., & Díaz-Sánchez, A. 2008, ApJ, 673, L185
Beuzit, J.-L., et al. 2004, A&A, 425, 997
Bildsten, L., Brown, E. F., Matzner, C. D., & Ushomirsky, G. 1997, ApJ, 482, 442
Bochanski, J. J., West, A. A., Hawley, S. L., & Covey, K. R. 2007, AJ, 133, 531
Bonfils, X., Delfosse, X., Udry, S., Santos, N. C., Forveille, T., & Ségransan, D. 2005, A&A, 442, 635
Bonnefoy, M., Chauvin, G., Rojo, P., Allard, F., Lagrange, A., Homeier, D., Dumas, C., & Beuzit, J. 2010, A&A, 512, A52
Borysow, A. 2002, A&A, 390, 779
Boss, A. P. 2006, ApJ, 637, L137
Bowler, B. P., Liu, M. C., & Cushing, M. C. 2009, ApJ, 706, 1114
Bowler, B. P., Liu, M. C., Dupuy, T. J., & Cushing, M. C. 2010, arXiv:1008.4582
Browning, M. K., Basri, G., Marcy, G. W., West, A. A., & Zhang, J. 2010, AJ, 139, 504
Burgasser, A. J. 2007, ApJ, 659, 655
Burgasser, A. J., Burrows, A., & Kirkpatrick, J. D. 2006a, ApJ, 639, 1095
Burgasser, A. J., Cruz, K. L., Cushing, M., Gelino, C. R., Looper, D. L., Faherty, J. K., Kirkpatrick, J. D., & Reid, I. N. 2010a, ApJ, 710, 1142
Burgasser, A. J., Cruz, K. L., & Kirkpatrick, J. D. 2007, ApJ, 657, 494
Burgasser, A. J., Geballe, T. R., Leggett, S. K., Kirkpatrick, J. D., & Golimowski, D. A. 2006b, ApJ, 637, 1067
Burgasser, A. J., Looper, D. L., Kirkpatrick, J. D., Cruz, K. L., & Swift, B. J. 2008a, ApJ, 674, 451
Burgasser, A. J., Looper, D., & Rayner, J. T. 2010b, AJ, 139, 2448
Burgasser, A. J., Marley, M. S., Ackerman, A. S., Saumon, D., Lodders, K., Dahn, C. C., Harris, H. C., & Kirkpatrick, J. D. 2002a, ApJ, 571, L151
Burgasser, A. J., Tinney, C. G., Cushing, M. C., Saumon, D., Marley, M. S., Bennett, C. S., & Kirkpatrick, J. D. 2008b, ApJ, 689, L53
Burgasser, A. J., et al. 2000, ApJ, 531, L57
Burgasser, A. J., et al. 2002b, ApJ, 564, 421
Burgasser, A. J., et al. 2003, ApJ, 592, 1186
Burgess, A. S. M., Moraux, E., Bouvier, J., Marmo, C., Albert, L., & Bouy, H. 2009, A&A, 508, 823
Burningham, B., et al. 2008, MNRAS, 391, 320
Burningham, B., et al. 2009, MNRAS, 395, 1237
Burningham, B., et al. 2010, MNRAS, 404, 1952
Burrows, A., Burgasser, A. J., Kirkpatrick, J. D., Liebert, J., Milsom, J. A., Sudarsky, D., & Hubeny, I. 2002, ApJ, 573, 394
Burrows, A., Sudarsky, D., & Hubeny, I. 2006, ApJ, 640, 1063
Burrows, A., & Volobuyev, M. 2003, ApJ, 583, 985
Casewell, S. L., Dobbie, P. D., Hodgkin, S. T., Moraux, E., Jameson, R. F., Hambly, N. C., Irwin, J., & Lodieu, N. 2007, MNRAS, 378, 1131
Chabrier, G., & Baraffe, I. 2000, ARA&A, 38, 337
Chabrier, G., Baraffe, I., Allard, F., & Hauschildt, P. 2000, ApJ, 542, 464
Chabrier, G., Baraffe, I., & Plez, B. 1996, ApJ, 459, L91
Chauvin, G., et al. 2005, A&A, 438, L29
Cooper, C. S., Sudarsky, D., Milsom, J. A., Lunine, J. I., & Burrows, A. 2003, ApJ, 586, 1320
Cushing, M. C., Rayner, J. T., & Vacca, W. D. 2005, ApJ, 623, 1115
Cushing, M. C., Saumon, D., & Marley, M. S. 2010, arXiv:1009.2802
Cushing, M. C., Vacca, W. D., & Rayner, J. T. 2004, PASP, 116, 362
Cushing, M. C., et al. 2006, ApJ, 648, 614
Cushing, M. C., et al. 2008, ApJ, 678, 1372

de Bruijne, J. H. J., Hoogerwerf, R., & de Zeeuw, P. T. 2001, A&A, 367, 111
Dehnen, W., & Binney, J. J. 1998, MNRAS, 298, 387
Delorme, P., et al. 2008, A&A, 484, 469
Dodson-Robinson, S. E., Veras, D., Ford, E. B., & Beichman, C. A. 2009, ApJ, 707, 79
Dupuy, T. J., Liu, M. C., & Ireland, M. J. 2009a, ApJ, 692, 729
Dupuy, T. J., Liu, M. C., & Ireland, M. J. 2009b, ApJ, 699, 168
Eggen, O. J. 1960, MNRAS, 120, 540
Faherty, J. K., Burgasser, A. J., Cruz, K. L., Shara, M. M., Walter, F. M., & Gelino, C. R. 2009, AJ, 137, 1
Famaey, B., Jorissen, A., Luri, X., Mayor, M., Udry, S., Dejonghe, H., & Turon, C. 2005, A&A, 430, 165
Feast, M., & Whitelock, P. 1997, MNRAS, 291, 683
Fegley, B. J., & Lodders, K. 1996, ApJ, 472, L37
Fleming, T. A., Schmitt, J. H. M. M., & Giampapa, M. S. 1995, ApJ, 450, 401
Freedman, R. S., Marley, M. S., & Lodders, K. 2008, ApJS, 174, 504
Geballe, T. R., Saumon, D., Leggett, S. K., Knapp, G. R., Marley, M. S., & Lodders, K. 2001, ApJ, 556, 373
Geballe, T. R., et al. 2002, ApJ, 564, 466
Gizis, J. E., & Harvin, J. 2006, AJ, 132, 2372
Goldman, B., Marsat, S., Henning, T., Clemens, C., & Greiner, J. 2010, MNRAS, 405, 1140
Golimowski, D. A., et al. 2004, AJ, 127, 3516
Greiner, J., et al. 2008, PASP, 120, 405
Griffith, C. A., & Yelle, R. V. 1999, ApJ, 519, L85
Helling, C., Dehn, M., Woitke, P., & Hauschildt, P. H. 2008, ApJ, 675, L105
Helling, C., Thi, W.-F., Woitke, P., & Fridlund, M. 2006, A&A, 451, L9
Hodapp, K. W., et al. 2003, PASP, 115, 1388
Høg, E., et al. 2000, A&A, 355, L27
Holman, M. J., & Wiegert, P. A. 1999, AJ, 117, 621
Houck, J. R., et al. 2004, ApJS, 154, 18
Hubeny, I., & Burrows, A. 2007, ApJ, 669, 1248
Janson, M., Bergfors, C., Goto, M., Brandner, W., & Lafrenière, D. 2010, ApJ, 710, L35
Johnson, J. A., & Apps, K. 2009, ApJ, 699, 933
Jones, H. R. A., & Tsuji, T. 1997, ApJ, 480, L39
Kalas, P., et al. 2008, Science, 322, 1345
Kiraga, M., & Stepien, K. 2007, Acta Astron., 57, 149
Kirkpatrick, J. D. 2005, ARA&A, 43, 195
Kirkpatrick, J. D., et al. 1999, ApJ, 519, 802
Kirkpatrick, J. D., et al. 2008, ApJ, 689, 1295
Knapp, G. R., et al. 2004, AJ, 127, 3553
Lafrenière, D., Jayawardhana, R., & van Kerkwijk, M. H. 2008, ApJ, 689, L153
Lafrenière, D., Jayawardhana, R., & van Kerkwijk, M. H. 2010, ApJ, 719, 497
Lagrange, A., et al. 2010, Science, 329, 57
Lawrence, A., et al. 2007, MNRAS, 379, 1599
Leggett, S. K., Marley, M. S., Freedman, R., Saumon, D., Liu, M. C., Geballe, T. R., Golimowski, D. A., & Stephens, D. C. 2007, ApJ, 667, 537
Leggett, S. K., et al. 2008, ApJ, 682, 1256
Leggett, S. K., et al. 2009, ApJ, 695, 1517
Leggett, S. K., et al. 2010, ApJ, 710, 1627
Linsky, J. L. 1969, ApJ, 156, 989
Liu, F., et al. 2008, Proc. SPIE, 7017, 16
Liu, M. C., Dupuy, T. J., & Leggett, S. K. 2010, ApJ, 722, 311
Lodders, K. 1999, ApJ, 519, 793
Lodders, K. 2002, ApJ, 577, 974
Lodders, K. 2003, ApJ, 591, 1220
Lodders, K., & Fegley, B. 2002, Icarus, 155, 393
Lodders, K., & Fegley, B., Jr. 2006, in Chemistry of Low Mass Substellar Objects, Astrophysics Update 2, ed. J. W. Mason (Heidelberg: Springer Verlag), 1
Looper, D. L., et al. 2008, ApJ, 686, 528
López-Santiago, J., Micela, G., & Montes, D. 2009, A&A, 499, 129
Luhman, K. L., et al. 2007, ApJ, 654, 570
Madsen, S. 2003, A&A, 401, 565
Magazzu, A., Martin, E. L., & Rebolo, R. 1993, ApJ, 404, L17
Marchi, S. 2007, ApJ, 666, 475
Marley, M. 2000, in ASP Conf. Ser. 212, From Giant Planets to Cool Stars, ed. C. A. Griffith & M. S. Marley (San Francisco, CA: ASP), 152
Marley, M. S., Saumon, D., & Goldblatt, C. 2010, ApJ, submitted (arXiv:1009.6217)
Marley, M. S., Seager, S., Saumon, D., Lodders, K., Ackerman, A. S., Freedman, R. S., & Fan, X. 2002, ApJ, 568, 335
Marois, C., Macintosh, B., Barman, T., Zuckerman, B., Song, I., Patience, J., Lafrenière, D., & Doyon, R. 2008, Science, 322, 1348
Marsh, K. A., Kirkpatrick, J. D., & Plavchan, P. 2010, ApJ, 709, L158
Martin, E. L., Rebolo, R., & Zapatero-Osorio, M. R. 1996, ApJ, 469, 706
McLean, I. S., McGovern, M. R., Burgasser, A. J., Kirkpatrick, J. D., Prato, L., & Kim, S. S. 2003, ApJ, 596, 561
McLean, I. S., Prato, L., McGovern, M. R., Burgasser, A. J., Kirkpatrick, J. D., Rice, E. L., & Kim, S. S. 2007, ApJ, 658, 1217
McPherson, A. M., et al. 2006, Proc. SPIE, 6267, 626707
Metchev, S. A., & Hillenbrand, L. A. 2006, ApJ, 651, 1166
Mohanty, S., Jayawardhana, R., Huélamo, N., & Mamajek, E. 2007, ApJ, 657, 1064
Montes, D., López-Santiago, J., Fernández-Figueroa, M. J., & Gálvez, M. C. 2001, A&A, 379, 976
Moorwood, A., et al. 1998, Messenger, 94, 7
Nakajima, T., Oppenheimer, B. R., Kulkarni, S. R., Golimowski, D. A., Matthews, K., & Durrance, S. T. 1995, Nature, 378, 463
Nelson, R. P. 2003, MNRAS, 345, 233
Nidever, D. L., Marcy, G. W., Butler, R. P., Fischer, D. A., & Vogt, S. S. 2002, ApJS, 141, 503
Perryman, M. A. C., et al. 1998, A&A, 331, 81
Pierens, A., & Nelson, R. P. 2008, A&A, 483, 633
Pinfield, D. J., Jones, H. R. A., Lucas, P. W., Kendall, T. R., Folkes, S. L., Day-Jones, A. C., Chappelle, R. J., & Steele, I. A. 2006, MNRAS, 368, 1281
Pizzolato, N., Maggio, A., Micela, G., Sciortino, S., & Ventura, P. 2003, A&A, 397, 147
Pollack, J. B., Hubickyj, O., Bodenheimer, P., Lissauer, J. J., Podolak, M., & Greenzweig, Y. 1996, Icarus, 124, 62
Reid, I. N., Hawley, S. L., & Gizis, J. E. 1995, AJ, 110, 1838
Saumon, D., Bergeron, P., Lunine, J. I., Hubbard, W. B., & Burrows, A. 1994, ApJ, 424, 333
Saumon, D., & Marley, M. S. 2008, ApJ, 689, 1327
Saumon, D., Marley, M. S., Cushing, M. C., Leggett, S. K., Roellig, T. L., Lodders, K., & Freedman, R. S. 2006, ApJ, 647, 552
Saumon, D., et al. 2007, ApJ, 656, 1136
Schlaufman, K. C., & Laughlin, G. 2010, A&A, 519, 105
Schmidt, S. J., West, A. A., Hawley, S. L., & Pineda, J. S. 2010, AJ, 139, 1808
Schmidt, T. O. B., Neuhäuser, R., Seifahrt, A., Vogt, N., Bedalov, A., Helling, C., Witte, S., & Hauschildt, P. H. 2008, A&A, 491, 311
Scholz, R. 2010a, A&A, 515, A92
Scholz, R. 2010b, A&A, 510, L8
Simcoe, R. A., et al. 2008, Proc. SPIE, 7014, 27
Simcoe, R. A., et al. 2010, Proc. SPIE, 7735, 38
Simons, D. A., & Tokunaga, A. 2002, PASP, 114, 169
Soter, S. 2006, AJ, 132, 2513
Spiegel, D. S., Burrows, A., & Milsom, J. A. 2010, ApJ, 722, 871
Stamatellos, D., & Whitworth, A. P. 2009, MNRAS, 392, 413
Stephens, D. C., et al. 2009, ApJ, 702, 154
Takeda, G., Ford, E. B., Sills, A., Rasio, F. A., Fischer, D. A., & Valenti, J. A. 2007, ApJS, 168, 297
Tinney, C. G., Burgasser, A. J., Kirkpatrick, J. D., & McElwain, M. W. 2005, AJ, 130, 2326
Tody, D. 1986, Proc. SPIE, 627, 733
Tokunaga, A. T., Simons, D. A., & Vacca, W. D. 2002, PASP, 114, 180
Tsuji, T. 2005, ApJ, 621, 1033
Tsuji, T., Ohnaka, K., & Aoki, W. 1999, ApJ, 520, L119
Vacca, W. D., Cushing, M. C., & Rayner, J. T. 2003, PASP, 115, 389
van Leeuwen, F. 2007, A&A, 474, 653
Veras, D., Crepp, J. R., & Ford, E. B. 2009, ApJ, 696, 1600
Visscher, C., Lodders, K., & Fegley, B. 2010, ApJ, 716, 1060
Voges, W., et al. 2000, IAU Circ., 7432, 3
Vorobyov, E. I., & Basu, S. 2010, ApJ, 714, L133
Vrba, F. J., et al. 2004, AJ, 127, 2948
Warren, S. J., et al. 2007, MNRAS, 381, 1400
West, A. A., Hawley, S. L., Bochanski, J. J., Covey, K. R., Reid, I. N., Dhital, S., Hilton, E. J., & Masuda, M. 2008, AJ, 135, 785
Witte, S., Helling, C., & Hauschildt, P. H. 2009, A&A, 506, 1367
Wright, G. S., et al. 2008, Proc. SPIE, 7010, 27
Yamamura, I., Tsuji, T., & Tanabe, T. 2010, ApJ, 722, 682
Zapatero Osorio, M. R., Béjar, V. J. S., Martín, E. L., Rebolo, R., Barrado, y., Navascués, D., Mundt, R., Eislöffel, J., & Caballero, J. A. 2002, ApJ, 578, 536
Zapatero Osorio, M. R., Lane, B. F., Pavlenko, Y., Martín, E. L., Britton, M., & Kulkarni, S. R. 2004, ApJ, 615, 958